

Common and Rare Fundus Diseases Identification Using Vision-Language Foundation Model with Knowledge of Over 400 Diseases

Meng Wang^{1,2#}, Tian Lin^{3#}, Kai Yu⁴, Aidi Lin³, Yuanyuan Peng⁵, Lianyu Wang⁶, Cheng Chen⁷, Ke Zou⁸, Huiyu Liang³, Man Chen³, Xue Yao³, Meiqin Zhang³, Binwei Huang³, Chaoxin Zheng³, Wei Chen³, Yilong Luo³, Yifan Chen³, Jingcheng Wang⁹, Yih Chung Tham^{1,2}, Dianbo Liu^{1,2}, Wendy Wong^{1,2}, Sahil Thakur¹⁰, Beau Fenner^{10,11}, Yanda Meng¹², Yukun Zhou^{13,14,15}, Zehua Jiang^{16,17}, Minghui Qiu¹⁸, Changqing Zhang¹⁹, Xinjian Chen²⁰, Sophia Y. Wang²¹, Cecilia S. Lee^{22,23}, Lucia Sobrin²⁴, Pearse A. Keane^{14,25}, Ching-Yu Cheng^{1,2,10,11(✉)}, Haoyu Chen^{3(✉)}, and Huazhu Fu^{26(✉)}

¹ Centre for Innovation & Precision Eye Health, Yong Loo Lin School of Medicine, National University of Singapore, Singapore 117549, Singapore.

² Department of Ophthalmology, Yong Loo Lin School of Medicine, National University of Singapore, Singapore 117549, Singapore.

³ Joint Shantou International Eye Center, Shantou University and the Chinese University of Hong Kong, 515041 Shantou, Guangdong, China.

⁴ Department of Radiology, University of Pennsylvania, Philadelphia, PA 19104, USA.

⁵ School of Biomedical Engineering, Anhui Medical University, 230032 Hefei, Anhui, China.

⁶ College of Computer Science and Technology, Nanjing University of Aeronautics and Astronautics, 211100 Nanjing, Jiangsu, China.

⁷ Center of Advanced Medical Computing and Analysis, Massachusetts General Hospital and Harvard Medical School, Boston, MA 02114, USA.

⁸ National Key Laboratory of Fundamental Science on Synthetic Vision and the College of Computer Science, Sichuan University, 610065 Chengdu, Sichuan, China.

⁹ Big Vision Medical Technology Ltd., Suzhou, China.

¹⁰ Singapore Eye Research Institute, Singapore National Eye Centre, Republic of Singapore.

¹¹ Ophthalmology & Visual Sciences Academic Clinical Program (EYE ACP), Duke-NUS Medical School, Singapore.

¹² Department of Computer Science, University of Exeter, Exeter, EX4 4RN, UK.

¹³ Centre for Medical Image Computing, University College London, London, UK.

¹⁴ NIHR Biomedical Research Centre at Moorfields Eye Hospital NHS Foundation Trust, London, UK.

¹⁵ Department of Medical Physics and Biomedical Engineering, University College London, London, UK.

¹⁶ Tsinghua Medicine of Tsinghua University, 100084, Beijing, China.

¹⁷ School of Clinical Medicine, Beijing Tsinghua Changgung Hospital, 102218, Beijing, China.

¹⁸ Foshan Aier Eye Hospital, 528000, Foshan, Guangdong, China.

¹⁹ College of Intelligence and Computing, Tianjin University, 300350 Tianjin, China.

²⁰ School of Electronics and Information Engineering, Soochow University, Jiangsu 215006, China.

²¹ Byers Eye Institute, Department of Ophthalmology, Stanford University School of Medicine, Palo Alto, California, USA.

²² Department of Ophthalmology, University of Washington, Seattle, WA, USA.

²³ Roger H. and Angie Karalis Johnson Retina Center, Seattle, WA, USA.

²⁴ Department of Ophthalmology, Massachusetts Eye and Ear, Harvard Medical School, Boston, MA, USA.

²⁵ Institute of Ophthalmology, University College London, London, UK.

²⁶ Institute of High Performance Computing (IHPC), Agency for Science, Technology and Research (A*STAR), 1 Fusionopolis Way, #16-16 Connexis, Singapore 138632, Republic of Singapore.

M. Wang, and T. Lin are the co-first authors.

✉ C.Y. Cheng, H. Chen, and H. Fu are the co-corresponding authors and contributed equally.

Abstract. The current retinal artificial intelligence models were trained using data with a limited category of diseases and limited knowledge. In this paper, we present a retinal vision-language foundation model (RetiZero) with knowledge of over 400 fundus diseases. Specifically, we collected 341,896 fundus images paired with text descriptions from 29 publicly available datasets, 180 ophthalmic books, and online resources, encompassing over 400 fundus diseases across multiple countries and ethnicities. RetiZero achieved outstanding performance across various downstream tasks, including zero-shot retinal disease recognition, image-to-image retrieval, internal domain and cross-domain retinal disease classification, and few-shot fine-tuning. Specially, in the zero-shot scenario, RetiZero achieved a Top5 score of 0.8430 and 0.7561 on 15 and 52 fundus diseases respectively. In the image-retrieval task, RetiZero achieved a Top5 score of 0.9500 and 0.8860 on 15 and 52 retinal diseases respectively. Furthermore, clinical evaluations by ophthalmology experts from different countries demonstrate that RetiZero can achieve performance comparable to experienced ophthalmologists using zero-shot and image retrieval methods without requiring model retraining. These capabilities of retinal disease identification strengthen our RetiZero foundation model in clinical implementation.

1 Introduction

Blindness and visual impairment represent a significant disease burden globally, impacting millions of individuals. Detection and timely treatment of ocular conditions, such as retinal and optic nerve diseases, are crucial for reducing severe and permanent damage. However, the insufficient availability of ophthalmic medical resources severely limits the prompt screening and treatment of retinal diseases. In recent years, artificial intelligence (AI)-based retinal disease screening systems have alleviated the workload on healthcare professionals to some extent, providing crucial technological support for the timely screening of retinal disease patients and referring for treatment. Nevertheless, most previous AI-based methods were customized for specific diseases, such as diabetic retinopathy (DR) [1, 2], glaucoma [3, 4], and retinopathy of prematurity (ROP) [5, 6]. Although several methods have been proposed for simultaneously screening multiple retinal diseases with promising performance [7, 8], most current AI models for ocular disease screening were trained on task-specific datasets, leading to inevitable errors in prediction when new data (ex., images acquired by different camera) or changes in tasks (ex., introducing new or rare categories). Furthermore, due to limited healthcare resources and the varying prevalence of retinal disease, collecting comprehensive datasets covering all retinal abnormalities is time-consuming and challenging. Consequently, most AI models were trained on limited data and disease categories, restricting their feature representation. Applying these models to different real-world settings or tasks requires extensive retraining with large datasets. Moreover, data quality and labeling issues further limit the widespread adoption of AI models in ophthalmic clinical settings.

Driven by abundant of big data and robust computing hardware, large foundation models (LFMs) have excelled in computer vision tasks [9, 10]. Pre-trained on massive datasets, LFMs provide rich feature support for downstream tasks like object detection [11], few-shot recognition [12], and zero-shot [13], etc. The first ophthalmic LFM, RETFound [14], introduced in 2023, was trained on large, unannotated retinal images using masked autoencoder (MAE) framework [15]. It provides rich feature support and improves the performance of downstream tasks, including internal domain and cross-domain retinal disease classification, few-shot learning, and prediction of systemic diseases. However, such an approach can hinder the model's capacity to align feature information with labels in downstream tasks. In contrast, the Foundation LLanguage-Image model of the Retina (FLAIR), a Contrastive Language-Image Pre-training (CLIP)-based LFMs enhance feature representation by aligning text descriptions with image features, improving feature-label alignment but struggling with complex semantic features in medical imaging [10]. Current LFMs for ophthalmic imaging are pre-trained on extensive yet categorically limited datasets. Therefore, developing LFMs with comprehensive ophthalmic disease knowledge is crucial for representing complex retinal features and enhancing downstream task performance. However, collecting massive and diverse ophthalmic data that covers a wide range of retinal diseases for pretraining remains a significant challenge.

To address these problems and challenges, we collected 341,896 fundus images paired with text descriptions from 29 publicly available datasets (containing 303,124 fundus images with labels), 180 ophthalmic books (2,3328 fundus images with text descriptions), and online resources (15,544 fundus image with text descriptions), encompassing over 400 retinal and optic nerve diseases across multiple countries/regions and ethnicities. As shown in **Figure 1**, RetiZero is based on a contrastive vision-language pretraining framework that integrates MAE-based pretraining knowledge and low-rank training methods. Moreover, we introduced an uncertainty vision-language feature calibration method using Dirichlet reparameterization within the contrastive vision-language pretraining framework, to further better align vision-language features in the high-dimensional embedding space. Consequently, RetiZero achieved superior performance in various downstream tasks, including zero-shot fundus disease recognition, image-to-image fundus disease retrieval, internal domain retinal disease identification, few-shot fine-tuning, and cross-domain fundus disease identification.

2 Results

2.1 Zero-shot fundus disease recognition

The biggest advantage of RetiZero is the capability of zero-shot learning, which enables RetiZero to recognize fundus diseases using only textual prompts, without needing to retrain or fine-tune the model with labeled fundus images. As shown in **Figure 2 (a)**, RetiZero achieved overall Top 1, Top 3, and Top 5 scores of 0.4421, 0.7024, 0.8404, respectively, for recognizing 15 common fundus diseases and normal condition of 30,089 fundus images (Eye-15 dataset), improved by 25.52%, 15.68%, and 15.61% over FLAIR (a recent VLM foundation model) [16], respectively. Furthermore, in the analysis of individual disease, RetiZero shows outstanding zero-shot capability in identifying most categories, especially for glaucoma (Top1: 0.7477, Top3: 0.9292, and Top5: 0.9718), Retinal Detachment (Top1: 0.7624, Top3: 0.9060, and Top5: 0.9628), and Retinitis Pigmentosa (Top1: 0.8190, Top3: 0.9533, and Top5: 0.9737) (**Supplementary Figure 1**). Additionally, to further validate RetiZero's zero-shot capability in more challenging clinical scenarios, we collected a more demanding dataset named EYE-52. This dataset comprises 7,007 fundus images from various ophthalmology clinics, covering 52 fundus diseases, many of which are extremely rare in clinical practice. The incidence/prevalence of each category in the EYE-52 dataset was shown in **Supplementary Table 3**. As depicted in **Figure 2 (b)**, RetiZero achieved overall Top1, Top3, and Top5 scores of 0.3595, 0.6259, and 0.7561, respectively, for recognizing the 52 types of fundus diseases in a zero-shot manner, providing superior performance compared FLAIR [16] (Top1: 0.0915, Top3: 0.2626, and Top5: 0.3398) and Random recognizing (Top1: 0.0294, Top3: 0.0882, and Top5: 0.1471). Furthermore,

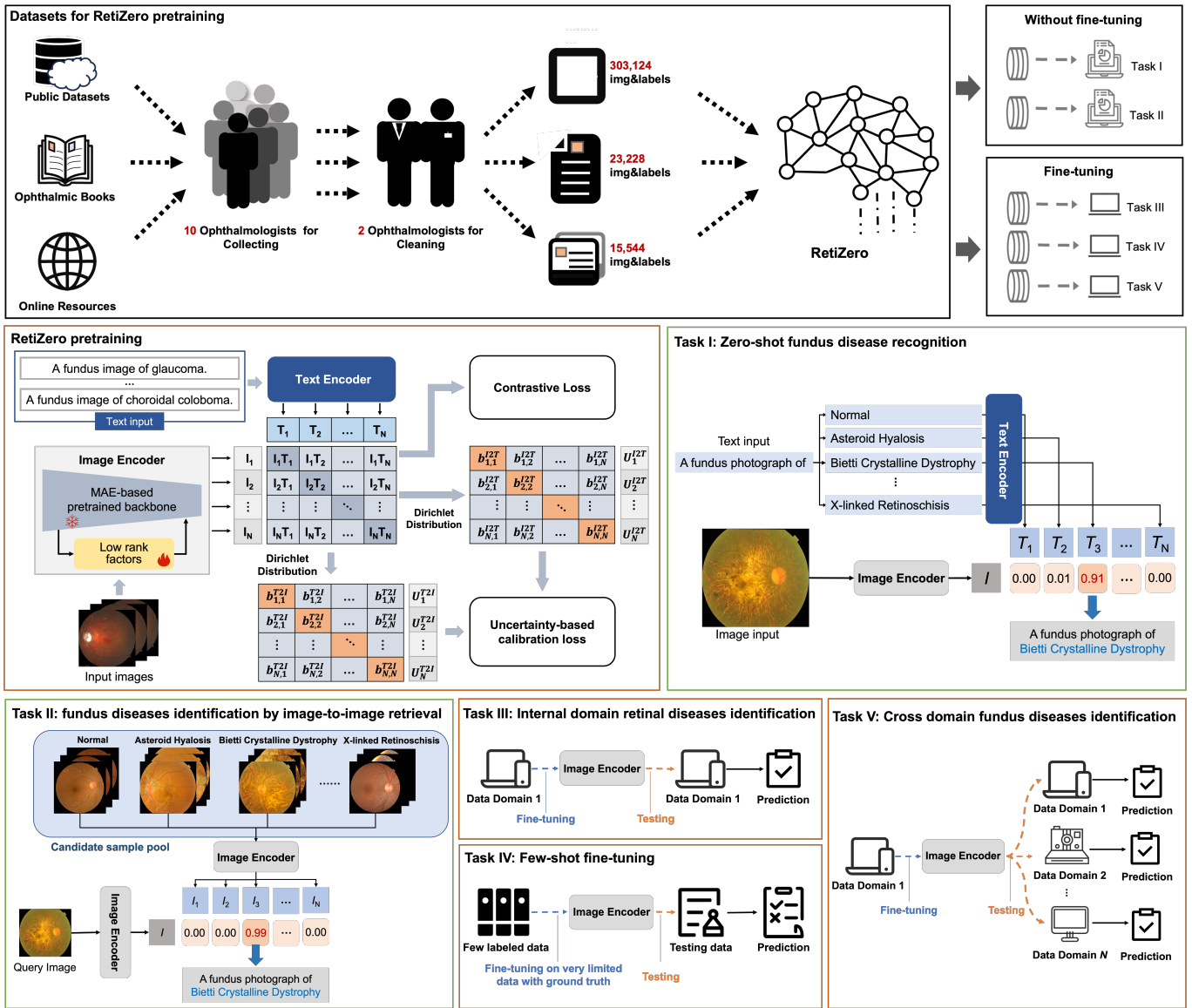


Figure 1. Overview of the framework. Datasets for RetiZero pretraining: The RetiZero model was pre-trained using data from three primary sources: public datasets, ophthalmologic books, and online resources. We assembled a team of 10 ophthalmologists for manual data collection, with an additional two members dedicated to data cleaning tasks. This involved downloading images and corresponding labels from public datasets, extracting images and text descriptions from ophthalmic books, and downloading retinal diseases-relevant images and text descriptions from online resources. RetiZero combines the strengths of self-supervised learning based on the MAE architecture and contrastive learning from the CLIP architecture. Moreover, we introduce an uncertainty vision-language feature calibration method into the contrastive vision-language pretraining framework, to further calibrate visual-language features in the high-dimensional embedding space. Task I: Zero-shot fundus disease recognition. Task II: Fundus disease identification by image-to-image retrieval. Task III: Internal domain retinal disease identification. "Internal domain" means that we fine-tuned and tested the model using the data with similar feature distribution. Task IV: Few-shot fine-tuning. We fine-tuned the model using a few training samples to evaluate RetiZero's performance in identifying fundus diseases with very limited training data. Task V: Cross-domain fundus disease identification. "Cross-domain" means that we fine-tuned and tested the model using the data with different feature distributions.

RetiZero demonstrated superior zero-shot performance, especially for recognizing some rare fundus diseases in clinical practice. For instance, RetiZero achieved Top 1, Top 3, and Top 5 scores of 0.6163, 0.7907, and 0.8605, respectively, for identifying Bietti Crystalline dystrophy. For the recognition of chorioretinal coloboma, the Top 1, Top 3, and Top 5 scores were 0.5085, 0.8079, and 0.9153, respectively (**Supplementary Figure 2**). **Figure 2 (c)** shows the Top5 prediction results provided by RetiZero and FLAIR for three rare disease samples. It can be seen that RetiZero's Top5 predictions include the correct disease, further demonstrating the outstanding performance of RetiZero in screening rare diseases. More details on the rest of the 52 disease categories can be found in **Supplementary Figure 2**.

2.2 Fundus disease identification by image-to-image retrieval

As shown in task II of **Figure 1**, we sequentially randomly sampled one image from the dataset as the query image and used the remaining samples as the candidate pool, then we computed the similarity scores between the features extracted by the image encoder of RetiZero from the query image and all candidate images. **Figure 2 (d)** and **Supplementary Figure 3** illustrated the excellent performance of RetiZero in identifying 15 fundus diseases through image-to-image retrieval. The overall scores for Top1, Top3, and Top5 are 0.8537, 0.9279, and 0.9500, respectively, representing an improvement of 9.35%, 4.79%, and 3.22% over RETFound [14], and 300.22%, 121.11%, 74.00% over FLAIR [16]. In addition, RetiZero demonstrated the best performance across all categories compared to RETFound [14] and FLAIR [16] (**Supplementary Figure 3**). Moreover, in the more challenging Eye-52 dataset, RetiZero achieved overall Top1, Top3, and Top5 scores of 0.7257, 0.8432, and 0.8860, respectively (**Figure 2 (e)**). Improved by 12.35%, 7.85%, and 6.30% over RETFound [14], and 767.75%, 389.88%, 271.51% over FLAIR [16], respectively. Furthermore, in analysis of individual disease, RetiZero demonstrated great potential, particularly in identifying several rare fundus diseases such as Bietti crystalline dystrophy (Top1: 0.8605, Top3: 0.9360, and Top5: 0.9419), chorioretinal coloboma (Top1: 0.8192, Top3: 0.8927, and Top5: 0.9096), and punctate inner choroidopathy multifocal choroiditis (Top1: 0.9022, Top3: 0.9464, and Top5: 0.9621) (**Supplementary Figure 4**). More details on the 52 disease categories can be found in **Supplementary Figure 4**. In addition, we also calculated Precision@1, Precision@3, and Precision@5 to comprehensively evaluate RetiZero's performance in the task of fundus disease identification through image-to-image retrieval. **Figures 2 (d)** and **Figures 2 (e)** demonstrate that RetiZero achieved the highest Precision@1, Precision@3, and Precision@5 on both testing datasets, EYE-15 and EYE-52. Meanwhile, RetiZero demonstrated the best performance across most categories compared to RETFound [14] and FLAIR [16] (**Supplementary Figure 5** and **Supplementary Figure 6**). Moreover, **Figure 2 (f)** shows an example of the Top5 prediction results from RetiZero, RETFound, and FLAIR. It can be seen that RetiZero achieved superior retrieval performance compared to RETFound and FLAIR, further demonstrating its excellent feature representation capabilities. Furthermore, **Supplementary Figure 7** presents heatmaps illustrating the weights of different foundational models for various fundus diseases. RetiZero's weights were more precisely concentrated on the regions affected by different fundus diseases. This precise focus underscores RetiZero's capability to accurately identify a range of fundus diseases, including rare ones, providing significant evidence of its diagnostic proficiency.

2.3 Clinical evaluation by ophthalmology experts from different countries

To comprehensively evaluate RetiZero's capability in fundus disease recognition without retraining the model, we randomly selected two samples from each category of the EYE-52 dataset, creating a new subset called EYE52-sub with a total of 104 instances. 14 ophthalmic experts from Singapore, the United States, and China were invited to diagnose the 104 samples in the EYE52-sub dataset. Among them, four ophthalmic experts have 3 to 5 years of clinical experience, six have 5 to 10 years of clinical experience, and four have more than 10 years. Specifically, we developed an online fundus image reading system and uploaded the 104 samples to the server, as shown in **Figure 3**. Mimicking the zero-shot setup, we provided 52 disease options on the webpage as prompts. During the image reading process, the clinicians selected diagnostic results from the 52 disease categories based on the image content. Finally, each expert was asked to assess their confidence in their diagnostic results. As shown in **Figure 3**, the diagnostic accuracy of the 14 ophthalmologists ranges from 0.365 to 0.788, and the median values between ophthalmologists is 0.582, while RetiZero's zero-shot Top1, Top3, and Top5 accuracies are 0.308, 0.635, and 0.798, respectively. Therefore, RetiZero's zero-shot Top3 performance is comparable to that of most ophthalmologists, and its Top5 performance surpasses that of all ophthalmologists. Furthermore, the fundus disease identification performance by image-to-image retrieval for RetiZero achieved Top1, Top3, and Top5 accuracies of 0.6837, 0.7449, and 0.7959, respectively. Therefore, RetiZero's Top1 accuracy in identifying fundus diseases through image-to-image retrieval surpasses that of most ophthalmologists. These experimental results further demonstrate that RetiZero can achieve performance comparable to experienced ophthalmologists through zero-shot and image retrieval methods without retraining the model.

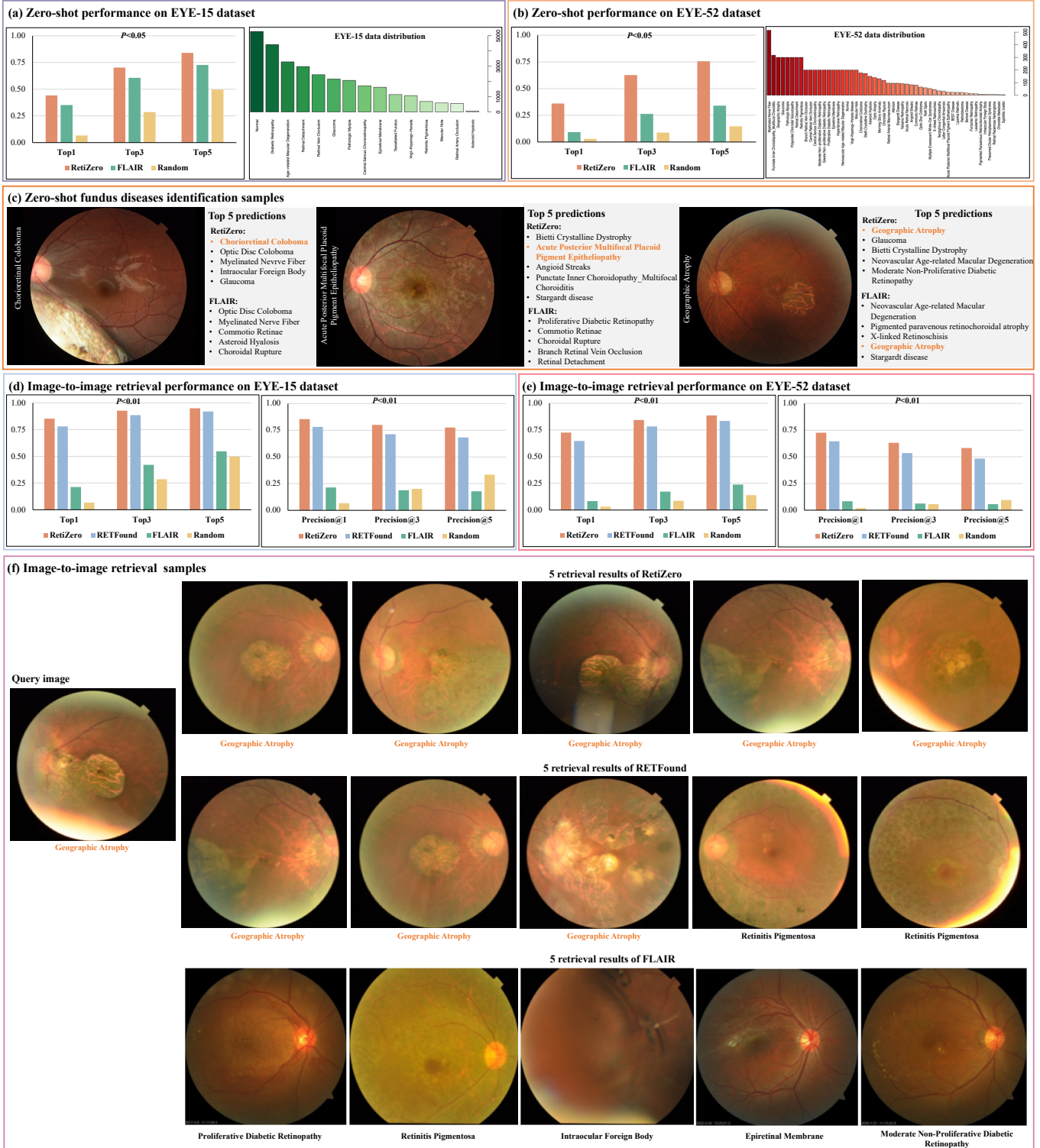


Figure 2. Overall Top1, Top3, and Top5 scores for zero-shot based fundus disease recognition and Fundus diseases identification by image-to-image retrieval. (a) The zero-shot performance on the EYE-15 dataset, which contains 30,089 fundus images including 14 common fundus diseases and a normal condition. (b) The zero-shot performance on the EYE-52 dataset, which contains 7,007 fundus images including 51 categories of fundus diseases and a normal condition. (c) Zero-shot fundus disease identification samples. (d) Image-to-image retrieval performance on EYE-15 dataset. (e) Image-to-image retrieval performance on the EYE-52 dataset. (f) Image-to-image retrieval samples. Supplementary Table 3 provides the incidence/prevalence of each category in the EYE-52 dataset.

2.4 Internal domain retinal disease identification

We collected three independent datasets from 5 ophthalmic clinics, named H1, H2, and H3, to validate the performance of RetiZero in internal domain retinal disease identification tasks. **Supplementary Figure 11** provides the data collection process and annotation details of three datasets. "Internal domain" means that we fine-tuned and validated the model separately within each of the three datasets. The details about three datasets as shown in **Supplementary Table 4** to **Supplementary Table 6**. As shown in **Figure 4 (a)**, RetiZero achieved average AUCs of 0.9972, 0.9796, and 0.9930 on the three datasets, respectively, each encompassing 15, 13, and 12 different categories of retinal diseases/normal condition, respectively. These results represent improvements of 1.90%, 6.94%, and 2.85% compared to RETFound [14], 1.06%, 7.97%, and 3.02% compared to FLAIR [16]. This is particularly evident for certain retinal diseases with ambiguous features, such as macular hole, epiretinal membrane, and retinal artery occlusion. RetiZero exhibited statistically significant improvement in the performance of identifying retinal diseases, demonstrating an obvious superiority over RETFound [14] and FLAIR [16] (all $p < 0.05$ in all of the three datasets, **Figure 4 (a)**).

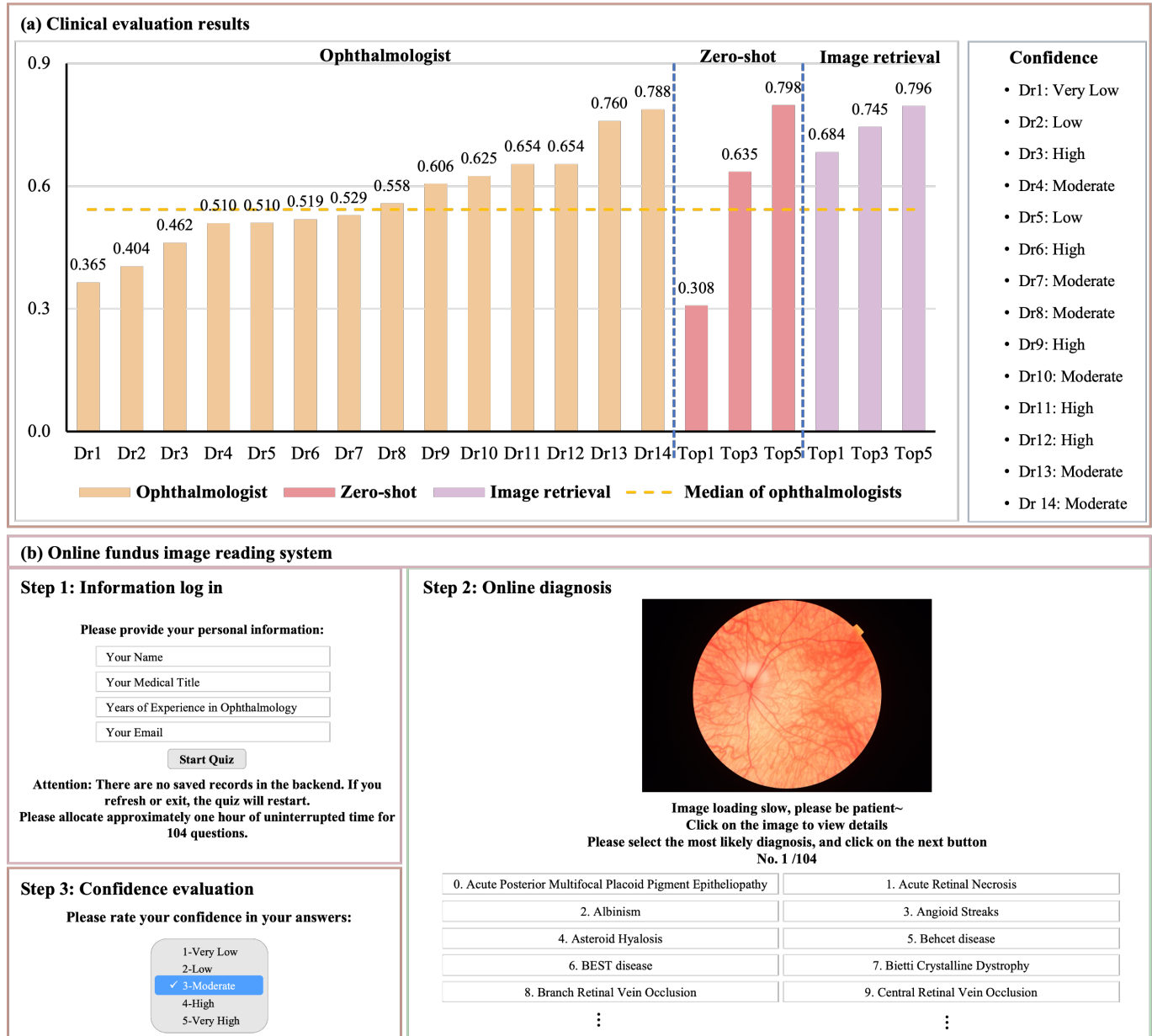


Figure: 3. Clinical evaluation. (a) Ophthalmologist diagnostic results, top1, top3 and top5 performance for zero-shot and image-to-image retrieval. (b) Our developed online fundus image reading system.

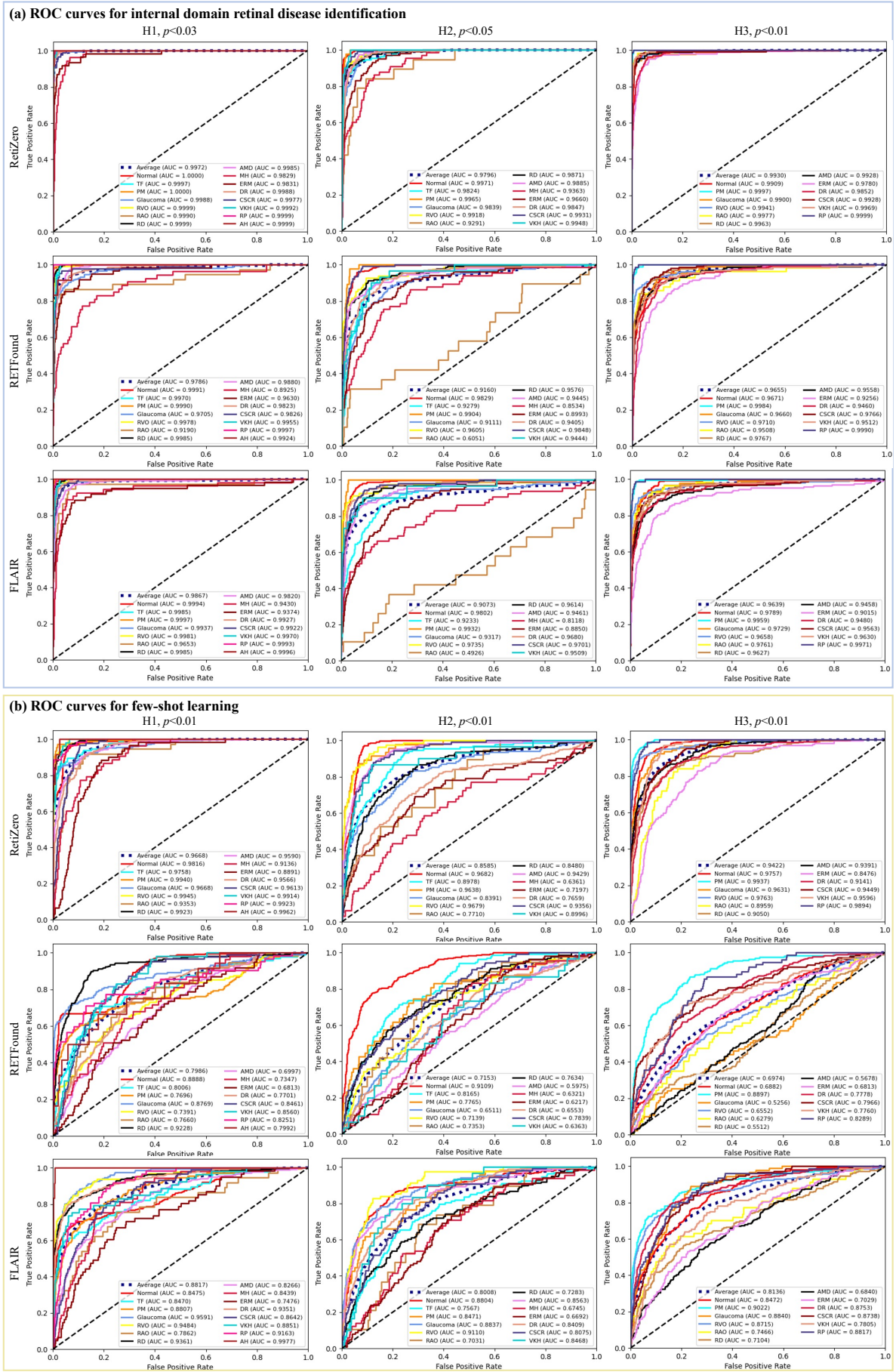


Figure: 4. The receiver operating characteristic (ROC) curves for internal domain retinal diseases identification and few-shot learning.

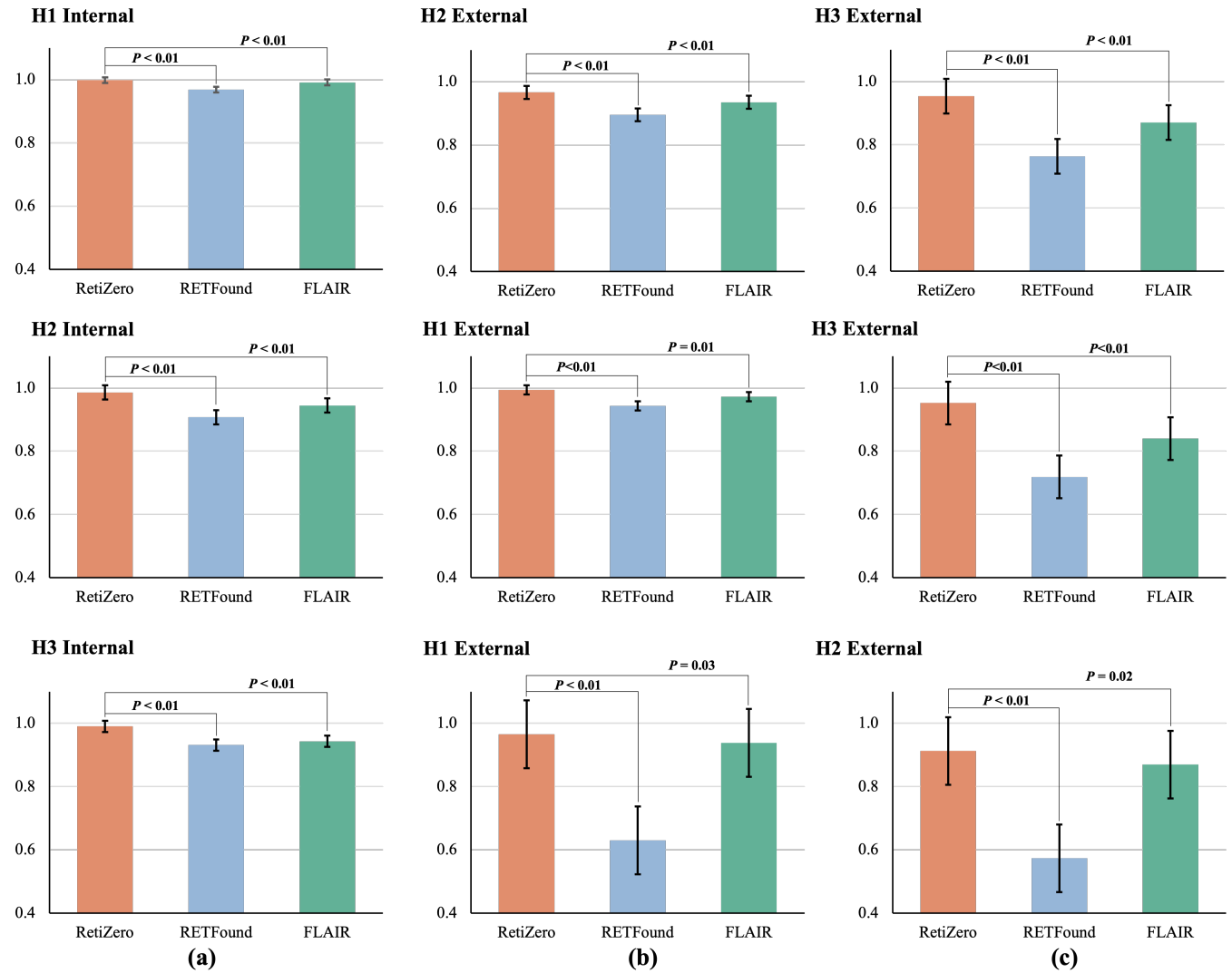


Figure 5. Cross-domain performance of different foundation models for fundus diseases screening. Column (a) Internal evaluation: Different foundation models were adapted to each dataset by fine-tuning and internally evaluated on hold-out testing data. Columns (b) and (c) Performance on external validation sets: The three foundation models were tested on the other two external validation datasets. The disease categories and dataset strategy information are listed in Supplementary Tables 10 to 12.

2.5 Few-shot fine-tuning

Limited annotated data has consistently hindered the advancement of AI algorithms for medical image recognition. To address the challenge, we fine-tuned the model using only five samples from each fundus disease to evaluate RetiZero’s performance in identifying fundus diseases with very limited training data. The data details were provided in **Supplementary Table 7 to Supplementary Table 9**. As shown in **Figure 4 (b)**, RetiZero achieved the highest AUROC scores across the three datasets compared to RETFound [14] and FLAIR [16]. In the task of identifying 15, 13, and 12 types of fundus diseases in the H1, H2, H3 dataset, RetiZero achieved AUROC values of 0.9668, 0.8585, and 0.9422 respectively, representing improvements of 7.21% to 35.10% over RETFound [14] and FLAIR [16] (all P -value < 0.01). These experimental results indicate that RetiZero possesses superior fundus feature representation capabilities. Even with limited annotated data samples, it can effectively learn the characteristic information of different fundus diseases in fundus images.

2.6 Cross domain fundus disease identification

To validate the robustness of RetiZero in the task of cross-domain fundus disease identification, we further reorganized the three datasets of H1, H2, and H3 and only used the data with shared categories across the three datasets. Then, we sequentially used the reorganized datasets of rH1, rH2, and rH3 as internal datasets and utilized the remaining two datasets as external testing sets to verify the robustness of different foundation models. The data information for

different experimental strategies is presented in **Supplementary Table 10 to 12**. As shown in **Figure 5**, RetiZero achieved promising performance in all validation settings. Specifically, in the internal test set of the three datasets, RetiZero achieved AUROC values of 0.9984, 0.9857, and 0.9901, respectively, representing improvements of 3.12%, 8.60%, and 6.32% over RETFound (all p-values < 0.01) [14]; 0.73%, 4.38%, and 4.97% over FLAIR (all P-values < 0.05, **Figure 5 (a)**) [16], with significant performance improvements observed in all testing set. In external tests, the performance of RetiZero remained similar to the internal test, with all AUROC ≥ 0.9124 and significantly outperformed RETFound [14] and FLAIR [16] in all tasks (all P-value ≤ 0.02 , **Figure 5 (b)** and **Figure 5 (c)**). Additionally, as shown in **Supplementary Figure 8** to **Supplementary Figure 10**, RetiZero exhibits different AUC scores in identifying various categories of retinal diseases on distinct datasets. Notably, RetiZero achieved outstanding performance in the identification of retinal diseases across most of the categories, especially in diseases with ambiguous pathologic features such as epiretinal membrane (ERM), retinal artery occlusion (RAO), and central serous chorioretinopathy (CSCR).

3 Discussion

In this study, we trained a vision-language-foundation model RetiZero for retinal imaging using vast fundus images paired with text description. It has demonstrated its strong capability in representing retinal disease features across a wide range of downstream tasks of retinal disease identification, including internal domain and cross-domain classification, few-shot fine-tuning, zero-shot recognition, and image-to-image retrieval. The performance of RetiZero is superior to two state-of-the-art LFM, RETFound [15] and FLAIR [16]. These results collectively demonstrated the superior generalizable and robust performance of RetiZero in both common and rare retinal disease identification.

The superiority of RetiZero over RETFound [14] and FLAIR [16] can be attributed to its unique design and diverse data used for pre-training. Although the RETFound model [14], pre-trained on a large number of fundus images using the MAE architecture, can enhance the performance of various downstream tasks, it included a limited number of fundus disease categories, particularly rare fundus diseases. In addition, it lacks the incorporation of textual information, resulting in insufficient characterization of image feature attributes, making it unsuitable for text prompt-based zero-shot fundus disease screening tasks and limiting its application in clinical practice scenarios, especially for the identification of rare fundus diseases. In contrast, FLAIR [16], based on the CLIP architecture, incorporates textual description information during network training to enhance the representation of image feature attributes. However, it is pre-trained on a very limited dataset of fundus disease knowledge, leading to poor performance in zero-shot recognition tasks for rare fundus diseases. Furthermore, FLAIR lacks guidance for learning information such as lesion contours and topological structures in images, resulting in low performance in fundus disease identification through image-to-image retrieval.

To address these limitations, we developed this fundus contrastive language-image foundation model, RetiZero, which integrates the strengths of MAE self-supervised learning and CLIP contrastive learning architectures. To further enhance the model's understanding of fundus diseases, we curated a dataset of image-text pairs covering over 400 fundus diseases, sourced from publicly available datasets, ophthalmic textbooks, and online resources for pretraining RetiZero. As a result, RetiZero is now a foundational model with extensive and comprehensive knowledge in ophthalmology.

Classification of retinal photographs for fundus disease identification is a well-studied task. Driven by comprehensive ophthalmic knowledge and contextual information from fundus images, RetiZero provides strong feature representation capability and robustness, enabling its superior performance for fundus disease identification across internal domain, cross-domain, and few-shot learning. Although the foundation model can reduce the sample size needed for training, classification tasks still require a certain number of images for fine-tuning and testing. It would be very challenging to collect enough sample sizes for rare diseases. To address this issue, we introduced image-to-image retrieval and zero-shot recognition tasks. Both tasks do not require data for fine-tuning, making them particularly useful for rare diseases. Image-to-image retrieval involves determining the category of a query fundus image based on feature similarity scores between the query and candidate images. RetiZero leverages its excellent image content representation capabilities of the MAE architecture and the textual feature alignment characteristics of the CLIP architecture. Therefore, it achieved superior performance in fundus disease retrieval tasks based on retinal image content. While the zero-shot learning setting allows for the recognition of rare diseases with as few as one sample. RetiZero learned textual knowledge of over 400 types of fundus diseases, enabling it to perform promisingly in zero-shot fundus disease recognition tasks, a feat not achievable by RETFound.

We also recognized limitations and the need for improvements in the current work. Although our collected dataset includes knowledge about over 400 types of fundus diseases, the imbalance across different categories may limit RetiZero's performance in downstream tasks. Therefore, further enriching the dataset with varied quantities of different categories of fundus diseases, especially for rare fundus diseases, will be part of our future work. In addition, while RetiZero has shown promising performance across multiple tasks and datasets, specialized models optimized for specific tasks may outperform generic models. Therefore, we will further explore improvements of RetiZero for specific tasks.

In conclusion, the proposed feature-calibrated retinal vision-language foundation model (RetiZero) with knowledge of over 400 retinal diseases can effectively represent the rich contextual feature information in fundus images, as well effectively learn the alignment between retinal image features and textual descriptions. RetiZero achieved superior performance on feature representation and generalizability across different retinal disease recognition tasks at various ophthalmic centers, different degrees of domain drift, and very limited training samples. Particularly, the outstanding

performance of RetiZero in zero-shot fundus disease identification and image-to-image retrieval-based fundus disease recognition holds significant importance for screening fundus diseases in clinical practice, especially for rare fundus diseases.

4 Methods

4.1 Dataset

Data for pretraining: We utilized RETFound [14], pre-trained on over 900,000 fundus images using the MAE architecture, as the pre-trained backbone for the Image Encoder of RetiZero. Meanwhile, we introduced low-rank learnable factors into the pre-trained RETFound and leveraged the CLIP architecture to learn image-text knowledge, aiming to enhance the model’s understanding of image-text correlations and improve its feature representation capabilities. We pre-trained RetiZero using our collected dataset comprising 341,896 image-text pairs, covering over 400 fundus diseases. Since the dataset used for pre-training with the MAE architecture has been previously described in RETFound [14], this paper focuses on detailing the 341,896 image-text dataset we collected. As shown in **Supplementary Table 13**, the image-text pretraining data mainly consists of three parts: publicly available dataset with category information, data from the ophthalmic books with description information, and data from online resources with description. Specifically, we collected a total of 303,129 fundus images from 29 publicly available datasets, covering over 100 different categories of retinal diseases. We used these category labels as textual descriptions corresponding to the fundus images input into RetiZero. To enable RetiZero to acquire a more comprehensive knowledge of ophthalmology, we invited 10 ophthalmologists to further collect 23,228 fundus images with corresponding textual descriptions from 180 ophthalmic books. As shown in **Supplementary Table 14**, these images cover 414 ophthalmic descriptive labels, encompassing nearly all known fundus diseases to date. Furthermore, we also collected 28,800 fundus data with relevant descriptions from the online resources. We assembled a team of 12 ophthalmologists to manually clean and organize 15,544 images along with their corresponding textual descriptions. In summary, the dataset for pretraining RetiZero covers almost all currently known fundus diseases, integrating very comprehensive ophthalmic knowledge. We pre-trained RetiZero on the public platform Pytorch and Nvidia Geforce DGX A100 GPU (80G). The batch size was set to 128. Adam was adopted as the optimizer to optimize RetiZero. The procedure of data collection for RetiZero pretraining was provided in Figure 1.

Data for internal domain retinal diseases identification: To verify the performance of the proposed RetiZero in the task of retinal disease identification, we built three datasets across multiple ophthalmic centers: health dataset 1 (H1), health dataset 2 (H2), and health dataset 3 (H3). This study was approved by the Joint Shantou International Eye Center Institutional Review Board and adhered to the principles of the Declaration of Helsinki. The data has been de-identified. In accordance with IRB regulations, if the data does not contain any identifiable patient information, informed consent is not required. As a result, this study has been granted approval to waive the need for informed consent. The clinical assessment and labeling procedure are shown in **Supplementary Figure 11**. H1 dataset, consists 11,414 fundus images covering 14 categories of retinal diseases and a normal condition, was collected from multiple eye clinics using different fundus cameras. We further divided H1 into training (6,942), validation (2,284), and testing (2,288) for model fine-tuning, model selection, and performance verification, respectively. More details of data information are given in **Supplementary Table 4**. H2 dataset consists of 7,812 fundus images, including 12 types of retinal diseases and 1 normal condition. The category and data information are given in **Supplementary Table 5**. To validate the performance of fine-tuning RetiZero for retinal disease identification on the H2 dataset, we partitioned the H2 dataset into training (4,682), validation (1,561), and testing (1,569) sets, respectively, for model fine-tuning, model selection, and performance evaluation. **Supplementary Table 6** provides the category and data distribution information for the H3 dataset, which comprises 10,863 fundus images across 12 categories. We divided the H3 dataset into training (6,511), validation (2,174), and testing (2,178) sets for model fine-tuning, selection, and performance evaluation. In this paper, we fine-tuned RetiZero to the task of internal domain retinal disease identification on the public platform Pytorch and Nvidia Geforce 3090 GPU (24). Adam optimizer and cross-entropy loss function were adopted to guide the model fine-tuning. The total iteration epoch and batch size were set to 100 and 64, respectively.

Data for few-shot fine-tuning: To evaluate the performance of RetiZero in the few-shot fine-tuning downstream task, we further reorganized the H1, H2, and H3 datasets. Specifically, we randomly selected 5 samples from each category of H1 training set, H2 training set, and H3 training set for few-shot fine-tuning, while retaining the validation and testing datasets for model selection and performance evaluation. More details about category and data distribution information are given in **Supplementary Table 7** to **Supplementary Table 9**. In this experiment, RetiZero was fine-tuned on the public platform Pytorch and Nvidia Geforce 3090 GPU (24G). Adam optimizer and cross-entropy loss function were adopted to guide the model optimization. The total iteration epoch and batch size were set to 1000 and 32, respectively.

Data for cross-domain fundus disease identification: To verify the generality and robustness of RetiZero in the task of cross-domain fundus disease identification, we invited professional doctors to re-organize the H1, H2, and H3

datasets. Ultimately, 11 overlapping categories were identified across the three datasets, which were then renamed as rH1 (10,304 fundus images), rH2 (6,829 fundus images), and rH3 (10,485 fundus images). As shown in **Supplementary Tables 10 to 12**, we conducted three experimental settings to validate the generality and robustness of RetiZero. Specifically, we sequentially adopted rH1, rH2, and rH3 as internal datasets for model fine-tuning, selection, and internal testing, while utilizing the remaining two datasets as external testing sets to assess the generality and robustness of RetiZero. Therefore, to deploy these experimental settings, we fine-tuned RetiZero on the public platform Pytorch and Nvidia Geforce 3090 GPUs (24G). We used the Adam optimizer and cross-entropy loss function to guide the model fine-tuning. The total iteration epochs and batch size were set to 100 and 64, respectively.

Data for the tasks of zero-shot fundus disease recognition and fundus disease identification by image-to-image retrieval: We combined three datasets from different hospitals, H1, H2, and H3, into a dataset named EYE-15, containing 30,089 fundus images that include 14 common fundus diseases and 1 normal category. This dataset was used to validate RetiZero’s performance in screening common fundus diseases in zero-shot and image-to-image retrieval approaches. The data distribution of each category in EYE-15 was provided in **Supplementary Table 1**. Moreover, we further collaborated with several ophthalmologists from multiple eye clinics to collect 7,007 fundus images by different fundus cameras (EYE-52 dataset), comprising 51 fundus diseases and 1 normal condition, to validate the performance of zero-shot fundus disease recognition and fundus disease identification by image-to-image retrieval in a more challenging setting. The data distribution was shown in **Supplementary Table 2**. As shown in **Supplementary Table 2**, EYE-52 comprises many clinically particularly rare fundus diseases, such as albinism, Bietti crystalline dystrophy, choroidal coloboma, and choroidal neoplasm. We adopted Top1, Top3, and Top 5 accuracy to evaluate the performance of RetiZero in both tasks of zero-shot fundus disease recognition and fundus disease identification by image-to-image retrieval. And, **Supplementary Figure 11** provides the process of the collection for the EYE-15 and EYE-52 datasets. In this paper, we also adopted Precision@1, Precision@3, and Precision@5 as the metrics to evaluate the performance of different foundation models in the task of fundus disease retrieval. Precision@N is a metric used to evaluate the performance of information retrieval systems and ranking algorithms. It is specifically used to measure the precision of the top N results returned by a system. Here is the formula and its explanation:

$$\text{Precision}@N = \frac{|R_{all} \cap R_{Re}@N|}{N}, \quad (1)$$

where R_{all} is the set of all relevant samples for the given query, $R_{Re}@N$ represents the set of the top N samples retrieved by the system in response to the query. $|R_{all} \cap R_{Re}@N|$ denotes the number of relevant samples in the top N retrieved documents, that is the count of samples that are both relevant and retrieved within the top N results, while N is the number of top samples considered for the calculation.

4.2 Framework of RetiZero

Figure 1 provides an overview of the RetiZero framework. RetiZero integrates the advantages of MAE self-supervised learning and CLIP contrastive learning architectures. Specifically, the model is built upon the MAE-based pre-trained backbone network RETFound [14], whose weights are frozen to preserve the model’s representation capability for complex semantic information such as lesion contours and topological structures in retinal images. Meanwhile, we introduced low-rank learnable factors into the pre-trained RETFound and leveraged the CLIP architecture to learn image-text knowledge, aiming to enhance the model’s understanding of image-text correlations and improve its feature representation capabilities. Furthermore, we incorporated an uncertainty vision-language feature calibration method based on Dirichlet reparameterization into the contrastive vision-language pretraining framework to further refine visual-language features in the high-dimensional embedding space, thereby enhancing the model’s ability to represent complex features in fundus images. Ultimately, RetiZero is obtained, which integrates the advantages of both MAE and CLIP architectures, providing feature support for subsequent downstream tasks. We will introduce the components of RetiZero in detail in the following sections.

Image Encoder: As shown in **Figure 1**, the image encoder consists of MAE-based SSL pre-trained backbone and low-rank learnable factors. MAE is a widely used self-supervised learning approach that employs a simple autoencoder approach to reconstruct the original signal based on partial observations. MAE-based SSL pretraining can guide the network to focus on the rich structural information and contextual features in the images. Therefore, RETFound [14], pre-trained on over 900,000 fundus images, is adopted as our MAE-based pre-trained backbone. Low-rank learnable factors (LoRA) are a parameter-efficient transfer learning method based on reparameterization [17], which utilizes low-rank representations to minimize the number of trainable parameters. It enables a pre-trained large foundation model to incorporate new knowledge into new target tasks, demonstrating robust and state-of-the-art (SOTA) performance in various parameter-efficient transfer learning tasks. Therefore, we utilize low-rank learnable factors to introduce retinal feature description information into the image encoder of RetiZero, enhancing its capacity to represent feature attributes of retinal images. Specifically, given the input token sequence $F_{in} \in R^{B \times N \times C_{in}}$ and the output token sequence $F_{out} \in R^{B \times N \times C_{out}}$ obtained by the projection layer $W \in R^{C_{out} \times C_{in}}$, LoRA assumes that updates to W should be gradual and stable. Therefore, we apply low-rank approximations to delineate this gradual update. First,

freeze the transformer layer to keep W fixed while adding a bypass to complete the low-rank approximation. And, the bypass consists of two linear mapping layers, $A \in R^{r \times C_{in}}$ and $B \in R^{C_{out} \times r}$, where $r \ll \{C_{in}, C_{out}\}$. Thus, the processing of the update layer \hat{W} can be described as:

$$F_{out} = \hat{W} F_{in}, \quad (2)$$

$$\hat{W} = W + \nabla W = W + BA. \quad (3)$$

Since the multi-head self-attention mechanism determines which regions to attend based on cosine similarity, LoRA was applied to the projection layers of query, key, or value to influence the attention scores. Therefore, we apply LoRA to the query and value projection layers for low-rank approximation optimization, thus the processing strategy for multi-head self-attention becomes:

$$Att(Q, K, V) = \text{Softmax} \left(\frac{QK^T}{\sqrt{C_{out}}} + B \right) V, \quad (4)$$

$$Q = \hat{W}_q F = W_q + B_q A_q F, \quad (5)$$

$$K = W_k F, \quad (6)$$

$$V = \hat{W}_v F = W_v F + B_v A_v F, \quad (7)$$

where W_q , W_k , and W_v are frozen projection layers of RETFound, while A_q , B_q , A_v , and B_v are trainable LORA factors.

Text Encoder: Descriptions of fundus images are typically more challenging than those of natural images, as they often contain numerous specialized clinical medical terms, sometimes even comprising multiple lesion signs or sentences. Therefore, in this paper, we utilize the BioClinicalBERT [18] model pre-trained on medical texts from the MIMIC III dataset as the text encoder to obtain clinically-aware textual embeddings.

4.3 Uncertainty-based feature calibration for guiding RetiZero pretraining

In this paper, we further introduced an uncertainty vision-language feature calibration method based on Dirichlet reparameterization [19, 20] into the contrastive vision-language pretraining framework, to further calibrate visual-language features in the high-dimensional embedding space for enhancing the robustness of the model to represent complex features in fundus images. Specifically, as shown in Figure 1, RetiZero’s pretraining consists of a fundus image encoder and a text encoder. The linear layer serves as a projection head for both the image encoder and the text encoder, mapping the acquired features to a 512-dimensional embedding feature space. Let assume $\phi = \{\phi_E, \phi_H\}$ denotes image encoder (ϕ_E) and corresponding projection head (ϕ_H). Given a fundus image X_i , the image encoder is adopted to obtain feature representation of $F_{Img} = \phi_E(X_i)$. Meanwhile, $\psi = \{\psi_E, \psi_H\}$ is used to represent text encoder (ψ_E) and corresponding projection head (ψ_H). The text encoder (ψ_E) is adopted to extract feature embedding $F_T = \psi_E(X_T)$ from text input X_T . Then, image projection head (ϕ_H) and text projection head (ψ_H) are utilized to map the independent modality representations into a joint unit hyper-sphere space: $I = \frac{\phi_H(F_{Img})}{\|\phi_H(F_{Img})\|}$ and $T = \frac{\psi_H(F_T)}{\|\psi_H(F_T)\|}$, respectively. The similarity between the input image (X_i) and input text (X_T) are evaluated by the cosine similarity based on the normalized features: $I^{Tr} T$, where Tr represents the transpose operator. With obtained similarity metrics, the optimization goal of the contrastive-based learning pre-training approach is to minimize the distance of features between paired images and text descriptions while maximizing the distance between features of unpaired samples. Specifically, assuming that a batch contains N samples, $I_i \in \{I_1, I_2, \dots, I_N\}$ and $T_i \in \{T_1, T_2, \dots, T_N\}$, represent image feature vector and text feature vector of each sample, while and $G = \{0, 1, \dots, N - 1\}$ is the corresponding category label, respectively. To guide model optimization, we use the following loss function.

$$L_{Con} = L_{Em} + L_{Di}, \quad (8)$$

$$L_{Em} = \frac{1}{2} \left(\sum_{i=1}^N -\log \left(\frac{\exp(I_i^{Tr} T_i)}{\sum_{k=1}^N \exp(I_k^{Tr} T_k)} \right) + \sum_{i=1}^N -\log \left(\frac{\exp(T_i^{Tr} I_i)}{\sum_{k=1}^N \exp(T_k^{Tr} I_k)} \right) \right), \quad (9)$$

L_{Di} is a loss function based on feature vectors which are reparametrized from similarity measures using the Dirichlet distribution. The specific implementation is as follows:

Step (1): Obtaining the evidence feature E_{I2T} and E_{T2I} by applying the Softplus activation function to similarity metrics between image and text feature embedding to ensure the feature values are larger than 0:

$$E_{I2T} = \text{Softplus}(I^{Tr} T), \text{ and } E_{T2I} = \text{Softplus}(T^{Tr} I), \quad (10)$$

where I2T and T2I indicate image-to-text and text-to-image contrastive direction.

Step (2): Parameterizing E_{I2T} and E_{T2I} to Dirichlet distribution, as:

$$\alpha_{I2T,k} = E_{I2T,k} + 1, \text{ i.e., } \alpha_{I2T,k} = e_{I2T,k} + 1, e_{I2T,k} = \{\text{Softmax}(I_k^{Tr}T_1), \dots, \text{Softmax}(I_k^{Tr}T_N)\}, \quad (11)$$

$$\alpha_{T2I,k} = E_{T2I,k} + 1, \text{ i.e., } \alpha_{T2I,k} = e_{T2I,k} + 1, e_{T2I,k} = \{\text{Softmax}(T_k^{Tr}I_1), \dots, \text{Softmax}(T_k^{Tr}I_N)\}, \quad (12)$$

where $\alpha_{I2T,k}$, $\alpha_{T2I,k}$, $e_{I2T,k}$, and $e_{T2I,k}$ are the k -th contrastive similarity Dirichlet distribution parameters and evidence for the image-text contrastive similarity of the k -th sample in a batch of N samples.

Step (3): Calculating the belief masses and corresponding uncertainty score as:

$$b_{I2T,k} = \frac{e_{I2T,k}}{S_{I2T}} = \frac{\alpha_{I2T,k} - 1}{S_{I2T}}, \quad u_{I2T} = \frac{N}{S_{I2T}}, \quad (13)$$

$$b_{T2I,k} = \frac{e_{T2I,k}}{S_{T2I}} = \frac{\alpha_{T2I,k} - 1}{S_{T2I}}, \quad u_{T2I} = \frac{N}{S_{T2I}}, \quad (14)$$

where $S_{I2T} = \sum_{k=1}^N (e_{I2T,k} + 1) = \sum_{k=1}^N \alpha_{I2T,k}$ and $S_{T2I} = \sum_{k=1}^N (e_{T2I,k} + 1) = \sum_{k=1}^N \alpha_{T2I,k}$ are the Dirichlet intensities of image-to-text and text-to-image, respectively, used to constrain $1 = \sum_{k=1}^N b_{I2T,k} + u_{I2T}$ and $1 = \sum_{k=1}^N b_{T2I,k} + u_{T2I}$. It can be seen from Eq. 13, and Eq. 14 the probability assigned to k -th sample is proportional to the observed similarity evidence for sample k . Conversely, if less total similarity evidence was obtained, the greater the total uncertainty.

In this study, we associate the Dirichlet distribution with the distribution of feature similarity between images and text descriptions, thereby obtaining belief masses and corresponding overall uncertainty score for the similarity of images and text description for each sample of a batch, based on the evidence collected from the feature similarity matrix. Therefore, we could work out the Dirichlet distribution parameter of $\alpha_{I2T} = [\alpha_{I2T,1}, \dots, \alpha_{I2T,N}]$ and $\alpha_{T2I} = [\alpha_{T2I,1}, \dots, \alpha_{T2I,N}]$ for image-to-text, and text-to-image, while obtaining the multinomial opinions $D(p_{I2T,i}|\alpha_{I2T,i})$ and $D(p_{T2I,i}|\alpha_{T2I,i})$, where $p_{I2T,i}$ and $p_{T2I,i}$ were the sample assignment probabilities on a simplex. Therefore, the loss function for the reparameterized similarity matrix as follows:

$$L_{Dl} = L_{Dl}^{I2T} + L_{Dl}^{T2I}, \quad (15)$$

where,

$$L_{Dl}^{I2T} = L_{Dl-CE}^{I2T} + \lambda * L_{KL}, \quad (16)$$

$$L_{Dl}^{T2I} = L_{Dl-CE}^{T2I} + \lambda * L_{KL}, \quad (17)$$

where L_{Dl-CE} (L_{Dl-CE}^{I2T} and L_{Dl-CE}^{T2I}) was used to ensure that the correct prediction for the sample with highest similarity between image and text yielded more evidence than other samples, while L_{KL} was used to ensure that incorrect predictions would yield less evidence, and λ was the balance factor that was gradually increased so as to prevent the model from paying too much attention to the KL divergence in the initial stage of training, which might result in a lack of good exploration of the parameter space and cause the network to output a flat uniform distribution.

$$L_{Dl-CE} = \int \left[\sum_{k=1}^N -y_k \log(p_k) \right] \frac{1}{\beta(\alpha_i)} \prod_{k=1}^N p_k^{\alpha_k - 1} dp_k = \sum_{k=1}^N y_k (\psi(S_k) - \psi(\alpha_k)), \quad (18)$$

where $\psi()$ was the digamma function, while $\beta()$ is the multinomial beta function for the concentration parameter α .

$$L_{KL} = \log \left(\frac{\Gamma\left(\sum_{k=1}^N \hat{\alpha}_k\right)}{\Gamma(N) \prod_{k=1}^N \Gamma\left(\sum_{k=1}^N \hat{\alpha}\right)} \right) + \sum_{k=1}^N (\hat{\alpha}_k - 1) \left[\psi(\hat{\alpha}_k) - \psi\left(\sum_{k=1}^N \hat{\alpha}_k\right) \right], \quad (19)$$

where $\hat{\alpha} = y + (1 - y) \odot \alpha$ is the adjusted parameter of the Dirichlet distribution which could avoid penalizing the evidence of the ground-truth class to 0, and $\Gamma()$ is the gamma function.

In general, as shown in Eq. 9 and Eq. 15 to Eq. 19, the loss function we designed can guide the network to focus on the feature differences in image-text similarity while further improving its robustness through mapping the features of the image-text similarity matrix to the Dirichlet distribution space to guide model optimization.

4.4 Definition of Dirichlet distribution

The Dirichlet distribution was parameterized by its concentration K parameters $\alpha = [\alpha_1, \dots, \alpha_K]$ [19, 20]. Therefore, the probability density function of the Dirichlet distribution was computed as:

$$D(P|\alpha) = \begin{cases} \frac{1}{\beta(\alpha)} \prod_{k=1}^K p_k^{\alpha_k - 1} & \text{for } P \in S_K \\ 0 & \text{Otherwise} \end{cases}, \quad (20)$$

where S_K was the K -dimensional unit simplex:

$$S_K = \left\{ P \mid \sum_{k=1}^K p_k = 1 \right\}, \quad 0 \leq p_k \leq 1, \quad (21)$$

where $\beta(\alpha)$ represented the K -dimensional multinomial beta function.

5 Code Availability

The code is available at <https://github.com/LooKing9218/RetiZero>.

6 Data Availability

The publicly available datasets used for pre-training are available at the following links and references:

APTOPS: <https://www.kaggle.com/c/aptos2019-blindness-detection>.

Cataract: <https://www.kaggle.com/datasets/jr2ngb/cataractdataset>.

DDR: <https://github.com/nkicsl/DDR-dataset>.

Diabetic Retinopathy Level Detection: <https://www.kaggle.com/datasets/arbethi/diabetic-retinopathy-level-detection>.

Diabetic Retinopathy Organized: <https://www.kaggle.com/datasets/dola1507108/diabetic-retinopathy-organized>.

DR15: https://www.kaggle.com/datasets/nawa393/dr15_test.

Messidor: <https://paperswithcode.com/dataset/messidor-1>.

MURED: <https://www.kaggle.com/datasets/abhirampolisetti/multi-label-retinal-disease-mured-dataset>.

Retina Dataset: <https://www.kaggle.com/datasets/jr2ngb/cataractdataset>.

Kaggle DR: <https://www.kaggle.com/c/diabetic-retinopathy-detection/data>.

ODIR5K: <https://www.kaggle.com/datasets/andrewmvd/ocular-disease-recognition-odir5k>.

ACRIMA [21], BEH [22], DeepDRID [23], DR1-2 [24], E-ophta [25], AIROGS [26], DeepEyeNet [27], FIVES [28], G1020 [29], Glaucoma dataset [30,31], IDRiD [32], JICHI [33], REFUGE [34], ORIGA [35], PARAGUAY [36], EyePACS AirDoc [37], JSIEC [8], RFMid [38]. Additional data sets supporting the findings of this study are not publicly available due to the confidentiality policy of the Chinese National Health Council and institutional patient privacy regulations. However, they are available from the corresponding authors upon request. For replication of the findings and/or further academic and AI-related research activities, data may be requested from the corresponding author H.C. (drchenhaoyu@gmail.com), and any requests will be responded to within 10 working days. Source data are provided in this paper.

References

1. V. Bellemo, Z. W. Lim, G. Lim, Q. D. Nguyen, Y. Xie, M. Y. Yip, H. Hamzah, J. Ho, X. Q. Lee, W. Hsu *et al.*, “Artificial intelligence using deep learning to screen for referable and vision-threatening diabetic retinopathy in africa: a clinical validation study,” *The Lancet Digital Health*, vol. 1, no. 1, pp. e35–e44, 2019.
2. Y. Xie, Q. D. Nguyen, H. Hamzah, G. Lim, V. Bellemo, D. V. Gunasekeran, M. Y. Yip, X. Q. Lee, W. Hsu, M. L. Lee *et al.*, “Artificial intelligence for teleophthalmology-based diabetic retinopathy screening in a national programme: an economic analysis modelling study,” *The Lancet Digital Health*, vol. 2, no. 5, pp. e240–e249, 2020.
3. M. Wang, L. Q. Shen, L. R. Pasquale, M. V. Boland, S. R. Wellik, C. G. De Moraes, J. S. Myers, T. D. Nguyen, R. Ritch, P. Ramulu *et al.*, “Artificial intelligence classification of central visual field patterns in glaucoma,” *Ophthalmology*, vol. 127, no. 6, pp. 731–738, 2020.
4. M. Wang, J. Tichelaar, L. R. Pasquale, L. Q. Shen, M. V. Boland, S. R. Wellik, C. G. De Moraes, J. S. Myers, P. Ramulu, M. Kwon *et al.*, “Characterization of central visual field loss in end-stage glaucoma by unsupervised artificial intelligence,” *JAMA ophthalmology*, vol. 138, no. 2, pp. 190–198, 2020.
5. Y. Peng, W. Zhu, Z. Chen, M. Wang, L. Geng, K. Yu, Y. Zhou, T. Wang, D. Xiang, F. Chen *et al.*, “Automatic staging for retinopathy of prematurity with deep feature fusion and ordinal classification strategy,” *IEEE Transactions on Medical Imaging*, vol. 40, no. 7, pp. 1750–1762, 2021.
6. S. Taylor, J. M. Brown, K. Gupta, J. P. Campbell, S. Ostmo, R. P. Chan, J. Dy, D. Erdogmus, S. Ioannidis, S. J. Kim *et al.*, “Monitoring disease progression with a quantitative severity scale for retinopathy of prematurity using deep learning,” *JAMA ophthalmology*, vol. 137, no. 9, pp. 1022–1028, 2019.
7. M. Wang, T. Lin, L. Wang, A. Lin, K. Zou, X. Xu, Y. Zhou, Y. Peng, Q. Meng, Y. Qian *et al.*, “Uncertainty-inspired open set learning for retinal anomaly identification,” *Nature Communications*, vol. 14, no. 1, p. 6757, 2023.
8. L.-P. Cen, J. Ji, J.-W. Lin, S.-T. Ju, H.-J. Lin, T.-P. Li, Y. Wang, J.-F. Yang, Y.-F. Liu, S. Tan *et al.*, “Automatic detection of 39 fundus diseases and conditions in retinal photographs using deep neural networks,” *Nature communications*, vol. 12, no. 1, p. 4828, 2021.
9. Z. Huang, F. Bianchi, M. Yuksekgonul, T. J. Montine, and J. Zou, “A visual–language foundation model for pathology image analysis using medical twitter,” *Nature medicine*, vol. 29, no. 9, pp. 2307–2316, 2023.
10. A. Radford, J. W. Kim, C. Hallacy, A. Ramesh, G. Goh, S. Agarwal, G. Sastry, A. Askell, P. Mishkin, J. Clark *et al.*, “Learning transferable visual models from natural language supervision,” in *International conference on machine learning*. PMLR, 2021, pp. 8748–8763.
11. M. Zhang, S. X. Fei, J. Liu, S. Xu, Y. Piao, and H. Lu, “Asymmetric two-stream architecture for accurate rgb-d saliency detection,” in *Computer Vision–ECCV 2020: 16th European Conference, Glasgow, UK, August 23–28, 2020, Proceedings, Part XXVIII 16*. Springer, 2020, pp. 374–390.
12. Z. Zhang, Y. Li, Q. Zhai, Y. Li, and M. Gao, “Few-shot learning for fine-grained signal modulation recognition based on foreground segmentation,” *IEEE Transactions on Vehicular Technology*, vol. 71, no. 3, pp. 2281–2292, 2022.

13. H. Lai, Q. Yao, Z. Jiang, R. Wang, Z. He, X. Tao, and S. K. Zhou, “Carzero: Cross-attention alignment for radiology zero-shot classification,” in *IEEE Conf. Comput. Vis. Pattern Recog.*, 2024.
14. Y. Zhou, M. A. Chia, S. K. Wagner, M. S. Ayhan, D. J. Williamson, R. R. Struyven, T. Liu, M. Xu, M. G. Lozano, P. Woodward-Court *et al.*, “A foundation model for generalizable disease detection from retinal images,” *Nature*, vol. 622, no. 7981, pp. 156–163, 2023.
15. K. He, X. Chen, S. Xie, Y. Li, P. Dollár, and R. Girshick, “Masked autoencoders are scalable vision learners,” in *Proceedings of the IEEE/CVF conference on computer vision and pattern recognition*, 2022, pp. 16 000–16 009.
16. J. Silva-Rodriguez, H. Chakor, R. Kobbi, J. Dolz, and I. B. Ayed, “A foundation language-image model of the retina (flair): Encoding expert knowledge in text supervision,” *arXiv preprint arXiv:2308.07898*, 2023.
17. E. J. Hu, Y. Shen, P. Wallis, Z. Allen-Zhu, Y. Li, S. Wang, L. Wang, and W. Chen, “Lora: Low-rank adaptation of large language models,” *arXiv preprint arXiv:2106.09685*, 2021.
18. E. Alsentzer, J. R. Murphy, W. Boag, W.-H. Weng, D. Jin, T. Naumann, and M. McDermott, “Publicly available clinical bert embeddings,” *arXiv preprint arXiv:1904.03323*, 2019.
19. Z. Han, C. Zhang, H. Fu, and J. T. Zhou, “Trusted multi-view classification,” in *International Conference on Learning Representations*, 2020.
20. K. W. Ng, G.-L. Tian, and M.-L. Tang, “Dirichlet and related distributions: Theory, methods and applications,” 2011.
21. A. Diaz-Pinto, S. Morales, V. Naranjo, T. Köhler, J. M. Mossi, and A. Navea, “Cnns for automatic glaucoma assessment using fundus images: an extensive validation,” *Biomedical engineering online*, vol. 18, pp. 1–19, 2019.
22. M. T. Islam, S. T. Mashfu, A. Faisal, S. C. Siam, I. T. Naheen, and R. Khan, “Deep learning-based glaucoma detection with cropped optic cup and disc and blood vessel segmentation,” *Ieee Access*, vol. 10, pp. 2828–2841, 2021.
23. R. Liu, X. Wang, Q. Wu, L. Dai, X. Fang, T. Yan, J. Son, S. Tang, J. Li, Z. Gao *et al.*, “Deepdrid: Diabetic retinopathy—grading and image quality estimation challenge,” *Patterns*, vol. 3, no. 6, 2022.
24. R. Pires, H. F. Jelinek, J. Wainer, E. Valle, and A. Rocha, “Advancing bag-of-visual-words representations for lesion classification in retinal images,” *PloS one*, vol. 9, no. 6, p. e96814, 2014.
25. E. Decenciere, G. Cazuguel, X. Zhang, G. Thibault, J.-C. Klein, F. Meyer, B. Marcotegui, G. Quellec, M. Lamard, R. Danno *et al.*, “Teleophta: Machine learning and image processing methods for teleophthalmology,” *Irbm*, vol. 34, no. 2, pp. 196–203, 2013.
26. C. De Vente, K. A. Vermeer, N. Jaccard, H. Wang, H. Sun, F. Khader, D. Truhn, T. Aimyshev, Y. Zhanibekuly, T.-D. Le *et al.*, “Airogs: artificial intelligence for robust glaucoma screening challenge,” *IEEE transactions on medical imaging*, 2023.
27. J.-H. Huang, C.-H. H. Yang, F. Liu, M. Tian, Y.-C. Liu, T.-W. Wu, I. Lin, K. Wang, H. Morikawa, H. Chang *et al.*, “Deepopht: medical report generation for retinal images via deep models and visual explanation,” in *Proceedings of the IEEE/CVF winter conference on applications of computer vision*, 2021, pp. 2442–2452.
28. K. Jin, X. Huang, J. Zhou, Y. Li, Y. Yan, Y. Sun, Q. Zhang, Y. Wang, and J. Ye, “Fives: A fundus image dataset for artificial intelligence based vessel segmentation,” *Scientific Data*, vol. 9, no. 1, p. 475, 2022.
29. M. N. Bajwa, G. A. P. Singh, W. Neumeier, M. I. Malik, A. Dengel, and S. Ahmed, “G1020: A benchmark retinal fundus image dataset for computer-aided glaucoma detection,” in *2020 International Joint Conference on Neural Networks (IJCNN)*. IEEE, 2020, pp. 1–7.
30. A. Singh, M. K. Dutta, M. ParthaSarathi, V. Uher, and R. Burget, “Image processing based automatic diagnosis of glaucoma using wavelet features of segmented optic disc from fundus image,” *Computer methods and programs in biomedicine*, vol. 124, pp. 108–120, 2016.
31. A. Issac, M. P. Sarathi, and M. K. Dutta, “An adaptive threshold based image processing technique for improved glaucoma detection and classification,” *Computer methods and programs in biomedicine*, vol. 122, no. 2, pp. 229–244, 2015.
32. P. Porwal, S. Pachade, M. Kokare, G. Deshmukh, J. Son, W. Bae, L. Liu, J. Wang, X. Liu, L. Gao *et al.*, “Idrid: Diabetic retinopathy—segmentation and grading challenge,” *Medical image analysis*, vol. 59, p. 101561, 2020.
33. H. Takahashi, H. Tampo, Y. Arai, Y. Inoue, and H. Kawashima, “Applying artificial intelligence to disease staging: Deep learning for improved staging of diabetic retinopathy,” *PloS one*, vol. 12, no. 6, p. e0179790, 2017.
34. J. I. Orlando, H. Fu, J. B. Breda, K. Van Keer, D. R. Bathula, A. Diaz-Pinto, R. Fang, P.-A. Heng, J. Kim, J. Lee *et al.*, “Refuge challenge: A unified framework for evaluating automated methods for glaucoma assessment from fundus photographs,” *Medical image analysis*, vol. 59, p. 101570, 2020.
35. Z. Zhang, F. S. Yin, J. Liu, W. K. Wong, N. M. Tan, B. H. Lee, J. Cheng, and T. Y. Wong, “Origa-light: An online retinal fundus image database for glaucoma analysis and research,” in *2010 Annual international conference of the IEEE engineering in medicine and biology*. IEEE, 2010, pp. 3065–3068.
36. V. E. C. Benítez, I. C. Matto, J. C. M. Román, J. L. V. Noguera, M. García-Torres, J. Ayala, D. P. Pinto-Roa, P. E. Gardel-Sotomayor, J. Facón, and S. A. Grillo, “Dataset from fundus images for the study of diabetic retinopathy,” *Data in brief*, vol. 36, p. 107068, 2021.
37. L. Ju, X. Wang, L. Wang, D. Mahapatra, X. Zhao, Q. Zhou, T. Liu, and Z. Ge, “Improving medical images classification with label noise using dual-uncertainty estimation,” *IEEE transactions on medical imaging*, vol. 41, no. 6, pp. 1533–1546, 2022.
38. S. Pachade, P. Porwal, D. Thulkar, M. Kokare, G. Deshmukh, V. Sahasrabuddhe, L. Giancardo, G. Quellec, and F. Mériaudeau, “Retinal fundus multi-disease image dataset (rfmid): A dataset for multi-disease detection research,” *Data*, vol. 6, no. 2, p. 14, 2021.

Supplementary files

Supplementary Table: 1. Data details of EYE-15 dataset.

Category	Number
Asteroid Hyalosis	60
Age-related Macular Degeneration	3,291
Central Serous Chorioretinopathy	1,715
Diabetic Retinopathy	4,422
Epiretinal Membrane	1,620
Glaucoma	2,160
Macular Hole	587
Normal	5,281
Pathologic Myopia	2,072
Retinal Artery Occlusion	560
Retinal Detachment	2,980
Retinitis Pigmentosa	685
Retinal Vein Occlusion	2,446
Tessellated Fundus	1,139
Vogt-Koyanagi-Harada	1,071
Total	30,089

Supplementary Table: 2. Data details of EYE-52 dataset.

Category	Number
Acute Posterior Multifocal Placoid Pigment Epitheliopathy	24
Acute Retinal Necrosis	89
Albinism	95
Angioid Streaks	83
Asteroid Hyalosis	150
Behcet disease	17
BEST disease	23
Bietti Crystalline Dystrophy	172
Branch Retinal Vein Occlusion	200
Central Retinal Vein Occlusion	200
Central Serous Chorioretinopathy	200
Chorioretinal Coloboma	177
Choroidal Metastasis	5
Choroidal Rupture	118
Commotio Retinae	80
Moderate Non-proliferative Diabetic Retinopathy	200
Severe Non-proliferative Diabetic Retinopathy	200
Proliferative Diabetic Retinopathy	200
Epiretinal Membrane	200
Geographic Atrophy	300
Glaucoma	300
Hypertensive Retinopathy	200
Intraocular Foreign Body	7
Leber Congenital Amaurosis	31
Leukemic Retinopathy	12
Lipemia Retinalis	22
Macular Hole	200
Morning Glory Anomaly	131
Multiple Evanescent White-Dot Syndromes	53
Myelinated Nerve Fiber	515
Neovascular Age-related Macular Degeneration	200
Normal	200
Optic Atrophy	140
Optic Disc Coloboma	65
Pathologic Myopia	300
Pigmented paravenous retinochoroidal atrophy	8
Polypoidal Choroidal Vasculopathy	300
Presumed Ocular Histoplasmosis Syndrome	6
Punctate Inner Choroidopathy _ Multifocal Choroiditis	317
Prutscher Retinopathy	13
Retinal Arterial Macroaneurysm	96
Retinal Detachment	300
Retinal Racemose Hemangioma	6
Retinitis Pigmentosa	300
Retinoblastoma	22
Roth Spots	59
Serpiginous Choroidopathy	35
Stargardt disease	95
Syphilitic Uveitis	4
Valsalva Retinopathy	92
Vogt-Koyanagi-Harada disease	200
X-linked Retinoschisis	45
Total	7,007

Supplementary Table: 3. Incidence/Prevalence of each category in EYE-52 dataset.

Category	Number	Incidence /Prevalence	Reference
Acute Posterior Multifocal Placoid Pigment Epitheliopathy	24	I: 0.15 /100,000	https://eyewiki.aao.org/Acute_Posterior_Multifocal_Placoid_Pigment_Epitheliopathy
Acute Retinal Necrosis	89	I: 0.063 /100,000	https://www.aao.org/eyenet/article/diagnosis-and-treatment-of-acute-retinal-necrosis
Albinism	95	P: 0.667~2 /100,000	https://eyewiki.aao.org/Albinism
Angioid Streaks	83	P: 6.5 /100,000	https://europepmc.org/article/med/37868801
Asteroid Hyalosis	150	P: 8 /1000	
Behcet disease	17	P: 0.12 /100,000	https://www.uptodate.com/contents/clinical-manifestations-and-diagnosis-of-behcet-syndrome
BEST disease	23	P: 0.787 /100,000	https://www.ncbi.nlm.nih.gov/pmc/articles/PMC10910552
Bielli Crystalline Dystrophy	172	P: 1.493 /100,000	https://medlineplus.gov/genetics/condition/bielli-crystalline-dystrophy/
Branch Retinal Vein Occlusion	200	P: 4.42 /1000	https://emedicine.medscape.com/article/1223498-overview
Central Retinal Vein Occlusion	200	P: 1~2 /1000	https://www.ncbi.nlm.nih.gov/pmc/articles/PMC3178209/
Central Serous Chorioretinopathy	200	P: 9.9 /100,000 in males and 1.7/100,000 in females	https://pubmed.ncbi.nlm.nih.gov/22788735
Chorioretinal Coloboma	177	P: 5~22 /100,000	https://eyewiki.aao.org/Coloboma
Choroidal Metastasis	5	P: 2.3% to 9.2% in patients with cancer	https://www.e-retina.or.kr/journal/view.html?doi=10.21561/jor.2020.5.1.52
Choroidal Rupture	118	P: ~10 /100,000	https://www.opticianonline.net/content/features/choroidal-rupture
Commotio Retinae	80	I: 2.6% in orbital trauma	https://link.springer.com/referenceworkentry/10.1007/978-3-642-35951-4_979-1
Moderate Non-proliferative Diabetic Retinopathy	200	P: 10.6% in DR	https://www.ncbi.nlm.nih.gov/pmc/articles/PMC9319242
Severe Non-proliferative Diabetic Retinopathy	200	P: 1.2% in DR	https://www.ncbi.nlm.nih.gov/pmc/articles/PMC9319242
Proliferative Diabetic Retinopathy	200	P: 9.9% in DR	https://www.ncbi.nlm.nih.gov/pmc/articles/PMC9319242
Epiretinal Membrane	200	P: 2~20% in various groups	https://emedicine.medscape.com/article/1223882-overview
Geographic Atrophy	300	P: 0.81%	https://www.reviewofoptometry.com/article/sizing-up-geographic-atrophy
Glaucoma	300	P: 3.54%	https://www.aoojournal.org/article/S0161-6420(14)00433-3/pdf
Hypertensive Retinopathy	200	P: 2~17% in various groups	https://eyewiki.aao.org/Hypertensive_Retinopathy
Intraocular Foreign Body	7	I: 0.16 /100,000	https://www.ncbi.nlm.nih.gov/books/NBK576415
Leber Congenital Amaurosis	31	P: 2~3 /100,000	https://eyewiki.aao.org/Leber_Congenital_Amaurosis
Leukemic Retinopathy	12	P: 9~90% in leukemia	https://www.ncbi.nlm.nih.gov/pmc/articles/PMC4687193
Lipemia Retinalis	22	P: 23% in chylomicron-aemia	https://en.wikipedia.org/wiki/Lipaemia_retinalis
Macular Hole	200	I: 0.33%	https://emedicine.medscape.com/article/1224320-overview
Morning Glory Anomaly	131	P: 2.6 /100,000	https://onlinelibrary.wiley.com/doi/full/10.1111/aos.12778
Multiple Evanscent White-Dot Syndromes	53	I: 0.45 /100,000	https://www.reviewofophthalmology.com/article/an-update-on-white-dot-syndromes

Myelinated Nerve Fiber	515	P: 0.57%	https://pubmed.ncbi.nlm.nih.gov/2338989
Neovascular Age-related Macular Degeneration	200	P: 3% in the oldest	https://www.ncbi.nlm.nih.gov/pmc/articles/PMC10262804
Normal	200	unknown	
Optic Atrophy	140	I: 2.86 /100,000	https://www.ncbi.nlm.nih.gov/books/NBK559130
Optic Disc Coloboma	65	P: 8.9 /100,000	https://pubmed.ncbi.nlm.nih.gov/30549247
Pathologic Myopia	300	P: 0.2-3.8%	https://eyewiki.aao.org/Pathologic_Myopia_(Myopic_Degeneration)
Pigmented paravenous retinochoroidal atrophy	8	P: <0.1 /100,000	https://www.orpha.net/en/disease/detail/251295
Polypoidal Choroidal Vasculopathy	300	P: 4~9.8% in presumed AMD	https://eyewiki.aao.org/Polypoidal_Choroidal_Vasculopathy#Prevalence_and_Incidence
Presumed Ocular Histoplasmosis Syndrome	6	I: 1.35 /100,000 in U.S.	https://www.ncbi.nlm.nih.gov/pmc/articles/PMC9361689
Punctate Inner Choroidopathy_Multifocal Choroiditis	317	I: 0.04 /100,000	https://www.ncbi.nlm.nih.gov/pmc/articles/PMC8675391
Perlscher Retinopathy	13	P: 0.024 /100,000	https://journals.lww.com/ajg/fulltext/2022/10002/s1815_perlscher_retinopathy__a_rare_clinical.1815.aspx
Retinal Arterial Macroaneurysm	96	P: 0.22 /1000	https://www.aao.org/eyenet/article/diagnosis-of-retinal-arterial-macroaneurysm
Retinal Detachment	300	I: 7.79 /100,000	https://www.ncbi.nlm.nih.gov/pmc/articles/PMC9922621
Retinal Racemose Hemangioma	6	unknown	https://www.aao.org/education/disease-review/retinal-hemangiomas
Retinitis Pigmentosa	300	P: 0.2~0.33 /1000	https://www.orpha.net/en/disease/detail/791
Retinoblastoma	22	P: 5~6.67 /100,000	https://www.ncbi.nlm.nih.gov/books/NBK1452
Roth Spots	59	P: <5% in infective endocarditis	https://www.ncbi.nlm.nih.gov/pmc/articles/PMC7417078/
Serpiginous Choroidopathy	35	P: 0.2~5% in uveitis	https://www.ncbi.nlm.nih.gov/pmc/articles/PMC6407399
Stargardt disease	95	P: 10~12.5 /100,000	https://www.orpha.net/en/disease/detail/827
Syphilitic Uveitis	4	I: 1.25 /1000 in syphilis cohort	https://www.tandfonline.com/doi/full/10.1080/22221751.2023.2290836
Valsalva Retinopathy	92	unkown	https://emedicine.medscape.com/article/1228106-overview?form=fpf
Vogt-Koyanagi-Harada disease	200	P: 1%-4% in U.S.	https://eyewiki.aao.org/Vogt-Koyanagi-Harada_Disease
X-linked Retinoschisis	45	P: 4~20 /100,000 in males	https://www.orpha.net/en/disease/detail/792
Total	7,007		

Supplementary Table: 4. Data distribution of H1.

Category	Training	Validation	Testing	Total
AH	36	12	12	60
AMD	865	289	289	1,443
CSCR	257	86	86	429
DR	996	332	333	1,661
ERM	180	60	61	301
Glaucoma	615	205	206	1,026
MH	159	53	53	265
Normal	1275	425	425	2,125
PM	517	173	173	863
RAO	109	37	37	183
RD	815	272	272	1,359
RP	184	61	62	307
RVO	390	130	130	650
TF	286	96	96	478
VKH	158	53	53	264
Total	6,842	2,284	2,288	11,414

AH: Asteroid Hyalosis, AMD: Age-related Macular Degeneration, CSCR: Central Serous Chorioretinopathy, DR: Diabetic Retinopathy, ERM: Epiretinal Membrane, MH: Macular Hole, PM: Pathologic Myopia, RAO: Retinal Artery Occlusion, RD: Retinal Detachment, RP: Retinitis Pigmentosa, RVO: Retinal Vein Occlusion, TF: Tessellated Fundus, VKH: Vogt-Koyanagi-Harada disease.

Supplementary Table: 5. Data distribution of H2.

Category	Training	Validation	Testing	Total
AMD	502	167	168	837
CSCR	320	107	107	534
DR	757	253	253	1,263
ERM	300	100	100	500
Glaucoma	409	136	137	682
MH	193	64	65	322
Normal	877	293	293	1,463
PM	138	46	47	231
RAO	56	19	19	94
RD	406	135	136	677
RVO	241	80	81	402
TF	396	132	133	661
VKH	87	29	30	146
Total	4,682	1,561	1,569	7,812

AMD: Age-related Macular Degeneration, CSCR: Central Serous Chorioretinopathy, DR: Diabetic Retinopathy, ERM: Epiretinal Membrane, MH: Macular Hole, PM: Pathologic Myopia, RAO: Retinal Artery Occlusion, RD: Retinal Detachment, RVO: Retinal Vein Occlusion, TF: Tessellated Fundus, VKH: Vogt-Koyanagi-Harada disease.

Supplementary Table: 6. Data distribution of H3.

Category	Training	Validation	Testing	Total
AMD	606	202	203	1,011
CSCR	451	150	151	752
DR	898	300	300	1,498
ERM	491	164	164	819
Glaucoma	271	90	91	452
Normal	1015	339	339	1,693
PM	586	196	196	978
RAO	169	57	57	283
RD	566	189	189	944
RP	226	76	76	378
RVO	836	279	279	1,394
VKH	396	132	133	661
Total	6,511	2,174	2,178	10,863

AMD: Age-related Macular Degeneration, CSCR: Central Serous Chorioretinopathy, DR: Diabetic Retinopathy, ERM: Epiretinal Membrane, PM: Pathologic Myoia, RAO: Retinal Artery Occlusion, RD: Retinal Detachment, RP: Retinitis Pigmentosa, RVO: Retinal Vein Occlusion, VKH: Vogt-Koyanagi-Harada disease.

Supplementary Table: 7. 5-Shot training strategy information in on H1 dataset.

Category	Training	Validation	Testing
AH	5	12	12
AMD	5	289	289
CSCR	5	86	86
DR	5	332	333
ERM	5	60	61
Glaucoma	5	205	206
MH	5	53	53
Normal	5	425	425
PM	5	173	173
RAO	5	37	37
RD	5	272	272
RP	5	61	62
RVO	5	130	130
TF	5	96	96
VKH	5	53	53
Total	75	2,284	2,288

AH: Asteroid Hyalosis, AMD: Age-related Macular Degeneration, CSCR: Central Serous Chorioretinopathy, DR: Diabetic Retinopathy, ERM: Epiretinal Membrane, MH: Macular Hole, PM: Pathologic Myopia, RAO: Retinal Artery Occlusion, RD: Retinal Detachment, RP: Retinitis Pigmentosa, RVO: Retinal Vein Occlusion, TF: Tessellated Fundus, VKH: Vogt-Koyanagi-Harada disease.

Supplementary Table: 8. 5-Shot training strategy information in on H2 dataset.

Category	Training	Validation	Testing
AMD	5	167	168
CSCR	5	107	107
DR	5	253	253
ERM	5	100	100
Glaucoma	5	136	137
MH	5	64	65
Normal	5	293	293
PM	5	46	47
RAO	5	19	19
RD	5	135	136
RVO	5	80	81
TF	5	132	133
VKH	5	29	30
Total	65	1,561	1,569

AMD: Age-related Macular Degeneration, CSCR: Central Serous Chorioretinopathy, DR: Diabetic Retinopathy, ERM: Epiretinal Membrane, MH: Macular Hole, PM: Pathologic Myopia, RAO: Retinal Artery Occlusion, RD: Retinal Detachment, RVO: Retinal Vein Occlusion, TF: Tessellated Fundus, VKH: Vogt-Koyanagi-Harada disease.

Supplementary Table: 9. 5-Shot training strategy information in on H3 dataset.

Category	Training	Validation	Testing
AMD	5	202	203
CSCR	5	150	151
DR	5	300	300
ERM	5	164	164
Glaucoma	5	90	91
Normal	5	339	339
PM	5	196	196
RAO	5	57	57
RD	5	189	189
RP	5	76	76
RVO	5	279	279
VKH	5	132	133
Total	60	2,174	2,178

AMD: Age-related Macular Degeneration, CSCR: Central Serous Chorioretinopathy, DR: Diabetic Retinopathy, ERM: Epiretinal Membrane, PM: Pathologic Myoia, RAO: Retinal Artery Occlusion, RD: Retinal Detachment, RP: Retinitis Pigmentosa, RVO: Retinal Vein Occlusion, VKH: Vogt-Koyanagi-Harada disease.

Supplementary Table: 10. Data distribution with rH1 as internal dataset and rH2 and rH3 as external test sets.

Category	rH1 internal dataset			rH2 external test set	rH3 external test set
	Training	Validation	Testing		
Normal	1,275	425	425	1,463	1,693
AMD	865	289	289	837	1,011
CSCR	257	86	86	534	752
DR	996	332	333	1,263	1,498
ERM	180	60	61	500	819
Glaucoma	615	205	206	682	452
PM	517	173	173	231	978
RAO	109	37	37	94	283
RD	815	272	272	677	944
RVO	390	130	130	402	1,394
VKH	158	53	53	146	661
Total	6,177	2,062	2,065	6,829	10,485

AMD age-related macular degeneration, CSCR central serous chorioretinopathy, DR diabetic retinopathy, ERM epiretinal membrane, PM pathological myopia, RAO retinal artery occlusion, RD retinal detachment, RVO retinal vein occlusion, VKH vogt-koyamagi-harada disease.

Supplementary Table: 11. Data distribution with rH2 as internal dataset and rH1 and rH3 as external test sets.

Category	rH1 internal dataset			rH2 external test set	rH3 external test set
	Training	Validation	Testing		
Normal	877	293	293	2,125	1,693
AMD	502	167	168	1,443	1,011
CSCR	320	107	107	429	752
DR	757	253	253	1,661	1,498
ERM	300	100	100	301	819
Glaucoma	409	136	137	1,026	452
PM	138	46	47	863	978
RAO	56	19	19	183	283
RD	406	135	136	1,359	944
RVO	241	80	81	650	1,394
VKH	87	29	30	264	661
Total	4,093	1,365	1,371	10,304	10,485

AMD age-related macular degeneration, CSCR central serous chorioretinopathy, DR diabetic retinopathy, ERM epiretinal membrane, PM pathological myopia, RAO retinal artery occlusion, RD retinal detachment, RVO retinal vein occlusion, VKH vogt-koyamagi-harada disease.

Supplementary Table: 12. Data distribution with rH3 as internal dataset and rH1 and rH2 as external test sets.

Category	rH1 internal dataset			rH2 external test set	rH3 external test set
	Training	Validation	Testing		
Normal	1,015	339	339	2,125	1,463
AMD	606	202	203	1,443	837
CSCR	451	150	151	429	534
DR	898	300	300	1,661	1,263
ERM	491	164	164	301	500
Glaucoma	271	90	91	1,026	682
PM	586	196	196	863	231
RAO	169	57	57	183	94
RD	566	189	189	1,359	677
RVO	836	279	279	650	402
VKH	396	132	133	264	146
Total	6,285	2,098	2,102	10,304	6,829

AMD age-related macular degeneration, CSCR central serous chorioretinopathy, DR diabetic retinopathy, ERM epiretinal membrane, PM pathological myopia, RAO retinal artery occlusion, RD retinal detachment, RVO retinal vein occlusion, VKH vogt-koyamagi-harada disease.

Supplementary Table: 13. Data details for RetiZero Pretraining.

No.	Dataset	Images	Diseases number	Source
1	ACRIMA	705	2	Diaz-Pinto A, Morales S, Naranjo V, et al. CNNs for automatic glaucoma assessment using fundus images: an extensive validation. Biomedical engineering online, 2019, 18:1-19.
2	APTOS	3,662	5	https://www.kaggle.com/c/aptos2019-blindness-detection
3	BEH	634	2	Islam M T, Mashfu S T, Faisal A, et al. Deep learning-based glaucoma detection with cropped optic cup and disc and blood vessel segmentation. Ieee Access, 2021, 10: 2828-2841.
4	Cataract	601	>4	https://www.kaggle.com/datasets/jr2nbg/cataractdataset
5	DDR	13,673	6	https://github.com/nkicsl/DDR-dataset
6	DeepDRiD	2,256	5	Liu R, Wang X, Wu Q, et al. Deepdrid:Diabetic retinopathy—grading and image quality estimation challenge. Patterns, 2022, 3(6).
7	Diabetic Retinopathy Level Detection	4,396	5	https://www.kaggle.com/datasets/arbethi/diabetic-retinopathy-level-detection
8	Diabetic Retinopathy Organized	35,128	5	https://www.kaggle.com/datasets/dola1507108/diabetic-retinopathy-organized
9	DR1-2	1,597	7	Pires R, Jelinek H F, Wainer J, et al. Advancing bag-of-visual-words representations for lesion classification in retinal images. PloS one, 2014, 9(6): e96814.
10	DR15	34,043	5	https://www.kaggle.com/datasets/nawa393/dr15_test
11	E-ophta	463	2	Decenciere E, Cazuguel G, Zhang X, et al. TeleOphta: Machine learning and image processing methods for teleophthalmology. Irbm, 2013, 34(2): 196-203.
12	AIROGS	101,433	2	De Vente C, Vermeer K A, Jaccard N, et al. AIROGS: artificial intelligence for robust glaucoma screening challenge. IEEE transactions on medical imaging, 2023.
13	DeepEyeNet	6,048	>=13	Huang J H, Yang C H H, Liu F, et al. Deepopht: medical report generation for retinal images via deep models and visual explanation. Proceedings of the IEEE/CVF winter conference on applications of computer vision. 2021: 2442-2452.
14	FIVES	800	6	Jin K, Huang X, Zhou J, et al. Fives: A fundus image dataset for artificial Intelligence based vessel segmentation. Scientific Data, 2022, 9(1): 475.
15	G1020	1020	2	Bajwa M N, Singh G A P, Neumeier W, et al. G1020: A benchmark retinal fundus image dataset for computer-aided glaucoma detection. 2020 International Joint Conference on Neural Networks (IJCNN). IEEE, 2020: 1-7.

16	Glaucoma dataset	364	2	Anushikha Singh, Malay Kishore Dutta, M.ParthaSarathi, Vaclav Uher and Radim Burget, "Image processing based automatic diagnosis of glaucoma using wavelet features of segmented optic disc from fundus image" Computer&methods and programs in biomedicine, Vol. 124, pp. 108–120, Feb. 2016, doi:10.1016/j.cmpb.2015.10.010. Ashish Issac, M.Partha Sarathi and Malay Kishore Dutta, "An adaptive threshold based image processing technique for improved glaucoma detection and classification" Computer methods and programs in biomedicine, Vol. 122 No. 2, pp. 229-244, Nov. 2015, doi: 10.1016/j.cmpb.2015.08.002.
17	IDRiD	516	5	Porwal P, Pachade S, Kokare M, et al. Idrid: Diabetic retinopathy—segmentation and grading challenge. Medical image analysis, 2020, 59: 101561.
18	JICHI	9,939	5	Takahashi H, Tampo H, Arai Y, et al. Applying artificial intelligence to disease staging: Deep learning for improved staging of diabetic retinopathy. PloS one, 2017, 12(6): e0179790.
19	Messidor	1,200	4	https://paperswithcode.com/dataset/messidor-1
20	MURED	2,208	9	https://www.kaggle.com/datasets/abhirampolisetti/multi-label-retinal-disease-mured-dataset
21	REFUGE	800	2	Orlando J I, Fu H, Breda J B, et al. Refuge challenge: A unified framework for evaluating automated methods for glaucoma assessment from fundus photographs. Medical image analysis, 2020, 59: 101570.
22	ORIGA	650	2	Zhang Z, Yin F S, Liu J, et al. Orig-a-light: An online retinal fundus image database for glaucoma analysis and research. 2010 Annual international conference of the IEEE engineering in medicine and biology. IEEE, 2010: 3065-3068.
23	PARAGUAY	757	7	Benítez V E C, Matto I C, Román J C M, et al. Dataset from fundus images for the study of diabetic retinopathy. Data in brief, 2021, 36: 107068.
24	Retina Dataset	601	>4	https://www.kaggle.com/datasets/jr2ngb/cataractdataset
25	Kaggle	35,126	5	https://www.kaggle.com/c/diabetic-retinopathy-detection/data
26	EyePACS AirDoc	33,978	53	Ju L, Wang X, Wang L, et al. Improving medical images classification with label noise using dual-uncertainty estimation. IEEE transactions on medical imaging, 2022, 41(6): 1533-1546.
27	JSIEC	1,000	39	Cen L P, Ji J, Lin J W, et al. Automatic detection of 39 fundus diseases and conditions in retinal photographs using deep neural networks. Nature communications, 2021, 12(1): 4828.
28	RFMid	2,531	46	Pachade S, Porwal P, Thulkar D, et al. Retinal fundus multi-disease image dataset (rfmid): A dataset for multi-disease detection research. Data, 2021, 6(2): 14.
29	ODIR5K	7,000	>=7	https://www.kaggle.com/datasets/andrewmvd/ocular-disease-recognition-odir5k
30	Ophthalmic Book	23,228	>400	180 Ophthalmic books
31	Online Resources	15,544		Online Resources
	Total			341,896

Supplementary Table: 14. Diseases category information of the data from 180 ophthalmic books.

No.	Ophthalmic labels	Number
1	Achromatopsia	1
2	Acute exudative polymorphous vitelliform maculopathy	32
3	Acute idiopathic blind spot enlargement	2
4	Acute Idiopathic Maculopathy (AIM)	23
5	Acute Macular Neuroretinopathy (AMN)	25
6	Acute Posterior Multifocal Placoid Pigment Epitheliopathy (APMPPE)	128
7	Acute Retinal Necrosis (ARN)	280
8	Acute Zonal Occult Outer Retinopathy (AZOOR)	37
9	Adult-Onset Foveomacular Vitelliform Dystrophy (AFVD)	30
10	Albinism	100
11	Alport retinopathy	4
12	Amblyopia	5
13	Amyloidosis	23
14	Anemic chorioretinopathy	34
15	Angioid streaks	153
16	Annular choroidal dystrophy	13
17	Anterior Ischemic Optic Neuropathy (AION)	51
18	Arc Welder's Maculopathy	2
19	Arteriosclerotic changes	1
20	Arteritic Anterior Ischemic Optic Neuropathy (AAION)	49
21	Asteroid hyalosis	23
22	Asteroid macular dystrophy	2
23	Autosomal Dominant Vitreoretinochoroidopathy	14
24	Behcet disease	137
25	Bergmeister papilla	18
26	Best disease	301
27	Bietti Crystalline Dystrophy (BCD)	47
28	Bilateral Diffuse Uveal Melanocytic Proliferation (BDUMP)	25
29	Birdshot chorioretinopathy	90
30	Blood–brain barrier disruption maculopathy	5
31	Blue cone monochromatism	1
32	Bothnia retinal dystrophy	8
33	Branch Retinal Atery Occlusion (BRAO)	190
34	Branch Retinal Vein Occlusion (BRVO)	326
35	Bull eye maculopathy	41
36	Cancer-associated retinopathy	2
37	Carotid-cavernous fistula	1
38	Central Areolar Choroidal Dystrophy (CACD)	57
39	Central Retinal Artery Occlusion (CRAO)	192
40	Central Retinal Vein Occlusion (CRVO)	337
41	Central Serous Chorioretinopathy (CSCR)	230
42	Cherry-red spot	34
43	Chikungunya retinitis	8
44	Chorioretinal atrophy	37
45	Chorioretinitis	60
46	Chorioretinitis sclopetaria	18
47	Choroidal coloboma	126
48	Choroidal degeneration	9
49	Choroidal detachment	60
50	Choroidal folds	81
51	Choroidal granuloma	33
52	Choroidal hemorrhage	21
53	Choroidal infarction	8
54	Choroidal infiltration	1
55	Choroidal lesion	24
56	Choroidal Neovascularization (CNV)	203
57	Choroidal nevus	165
58	Choroidal rupture	95

59	Choroidal scar	4
60	Choroidal sclerosis	3
61	Choroidal tubercle	36
62	Choroideremia	114
63	Choroiditis	96
64	Chronic granulomatous disease	3
65	Cilioretinal artery occlusion	33
66	Coats disease	208
67	Cobblestone degeneration	14
68	Combined retinal artery and vein occlusion (RAVO)	17
69	Commotio Retinae	60
70	Compressive optic neuropathy	10
71	Cone-rod dystrophy	139
72	Congenital achromatopsia	2
73	Congenital grouped retinal pigment epithelium albinotic nevi	7
74	Congenital Hyper trophy of the Retinal Pigment Epithelium (CHRPE)	208
75	Congenital optic disc pigmentation	2
76	Congenital retinal macrovessels	8
77	Contusion injury	18
78	Cotton Wool Spots (CWS)	41
79	Crystalline retinopathy	33
80	Cuticular drusen	5
81	Cystoid degeneration	3
82	Dalen-Fuchs nodule	2
83	Dark without pressure	1
84	Decompression retinopathy	7
85	Diffuse Unilateral Subacute Neuroretinitis (DUSN)	91
86	Disciform lesions	3
87	Dislocated lens	25
88	Doyne Honeycomb Retinal Dystrophy (DHRD)	84
89	Dragged vessels	5
90	Drusen	223
91	Drusenoid PED	2
92	Dry Age-related Macular Degeneration (dry AMD)	160
93	Eales disease	84
94	Endophthalmitis	52
95	Enhanced S Cone Syndrome (ESCS)	17
96	Enlarged optic cup	2
97	Epiretinal Membrane (ERM)	243
98	Erosive vitreoretinopathy	5
99	Exudative retinal detachment	35
100	Familial dominant drusen	3
101	Familial Exudative Vitreoretinopathy (FEVR)	148
102	Familial Flecked Retina syndrome	33
103	Familial internal limiting membrane dystrophy	8
104	Familial optic neuropathy	11
105	Foveal hypoplasia	10
106	Frosted-branch angiitis	51
107	Fundus Albipunctatus	42
108	Fundus Flavimaculatus	30
109	fundus heterochromia	1
110	Gas bubble	22
111	Geographic Helicoid Peripapillary Choroidopathy (GHPC)	5
112	Giant Retinal Tear (GRT)	19
113	Glaucoma	154
114	Glob perforation	1
115	Goldmann-Favre disease	9
116	Granuloma	19
117	Gyrate Atrophy	72
118	Hamartoma	19

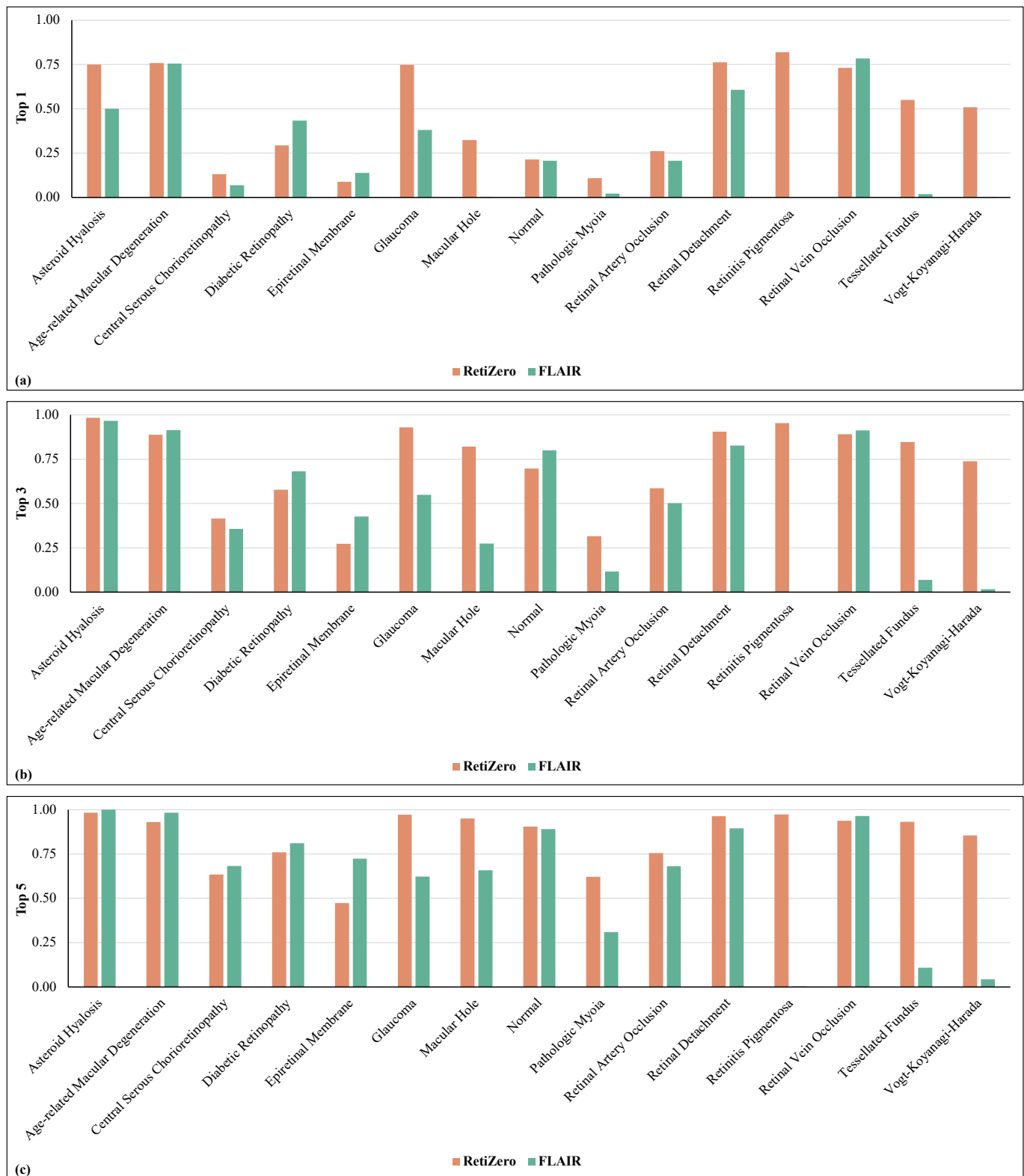
119	Hard exudate	22
120	Heavy liquid droplet	5
121	Hemangioblastoma	34
122	High-altitude retinopathy	3
123	Hyperlipidemia	7
124	Hyperoxaluria	7
125	Hypertensive retinopathy	229
126	Hyperviscosity syndrome	3
127	Hypotony retinopathy	25
128	Idiopathic obliterative arteritis	4
129	Idiopathic sclerochoroidal calcification	7
130	Idiopathic vasculitis Aneurysms and Neuroretinitis syndrome (IRVAN)	24
131	Incontinentia pigmenti	60
132	Infection	226
133	Infection Angiostrongyliasis	2
134	Infection Calliphoridae	4
135	Infection Candidiasis	76
136	Infection Cat-Scratch Disease	78
137	Infection CMV retinitis	236
138	Infection Coccidiomycosis	9
139	Infection Cryptococcosis	6
140	Infection Cysticercosis	74
141	Infection Dengue retinopathy	21
142	Infection Filariasis	4
143	Infection Gnathostomiasis	5
144	Infection HIV retinopathy	57
145	Infection Lyme disease	3
146	Infection Malaria retinopathy	3
147	Infection Nematode	4
148	Infection Onchocerciasis	2
149	Infection Ophthalmomyiasis interna	16
150	Infection Presumed Ocular Histoplasmosis syndrome (POHS)	184
151	Infection Rift Valley fever retinitis	5
152	Infection Rubella retinopathy	17
153	Infection Syphilis	15
154	Infection syphilitic chorioretinopathy	112
155	Infection Toxocariasis	116
156	Infection Toxoplasmosis	342
157	Infection Trematode	8
158	Infection Tuberculosis	24
159	Intermediate uveitis	106
160	Intraocular Foreign Body (IOFB)	68
161	Intraocular Garamycin	9
162	Laser spots	45
163	Late-onset retinal macular degeneration (LORMD)	5
164	Lattice degeneration	113
165	Leber Congenital Amaurosis (LCA)	65
166	Leber Hereditary Optic Neuropathy (LHON)	46
167	Leber idiopathic stellate neuroretinitis	25
168	Leber miliary aneurysm	6
169	Leukemic retinopathy	157
170	Lipemia retinitis	14
171	Lipid deposition	1
172	Luetic chorioretinitis	11
173	Lupus retinopathy	76
174	Lymphoma	206
175	Macropapilla	1
176	Macular atrophy	8
177	Macular dysplasia	1
178	Macular dystrophy	44

179	Macular edema	82
180	Macular Hole (MH)	247
181	Macular infarction syndrome	1
182	Macular scar	1
183	Macular telangiectasia	60
184	Maternally inherited diabetes and deafness (MIDD)	6
185	Megalopapilla	10
186	Microcystoid degeneration	2
187	micropapilla	1
188	Microphthalmos	1
189	Mitochondrial retinal Dystrophy	7
190	Morning Glory syndrome (MGS)	83
191	Multifocal Choroiditis (MFC)	115
192	Multiple Evanescence White Dot Syndrome (MEWDS)	67
193	Myelinated Nerve Fiber (MNF)	90
194	Myopia	46
195	Nanophthalmos	1
196	Neovascular Age-related Macular Degeneration (nAMD)	320
197	Neovascularization	59
198	Neuroretinitis	72
199	Newfoundland rod-cone degeneration (NFRCD)	3
200	Nicotinic acid maculopathy	2
201	Nonarteritic Anterior Ischemic Optic Neuropathy (NAION)	72
202	Non-Proliferative Diabetic Retinopathy (NPDR)	363
203	Normal	186
204	Norrie Disease	4
205	North Carolina Macular Dystrophy (NCMD)	108
206	Ocular Ischemic Syndrome (OIS)	68
207	Ocular melanocytosis	5
208	Ophthalmic artery occlusion	8
209	Optic disc anomaly	30
210	Optic disc aplasia	3
211	Optic disc atrophy	172
212	Optic disc avulsion	29
213	Optic disc coloboma	72
214	Optic disc drusen	82
215	Optic disc dysplasia	3
216	Optic disc granuloma	11
217	Optic disc hemorrhage	11
218	Optic disc hyaline body	15
219	Optic disc hypoplasia	65
220	Optic disc metastasis	21
221	Optic disc pallor	29
222	Optic disc pit	130
223	Optic neuritis	89
224	Optic neuropathy	12
225	Outer retinal corrugation	4
226	Overlapping WDS	10
227	Panuveitis	3
228	Papilloedema	332
229	Papillomegaly	8
230	Papillophlebitis	6
231	Papillorenal syndrome	13
232	Paraneoplastic vitelliform dystrophy	2
233	Paraneoplastic-Related Retinopathy	11
234	Pathological Myopia (PM)	692
235	Pattern Dystrophy	152
236	Pearl degeneration	1
237	Peripapillary atrophy	2
238	Peripheral exudative hemorrhagic chorioretinopathy	9

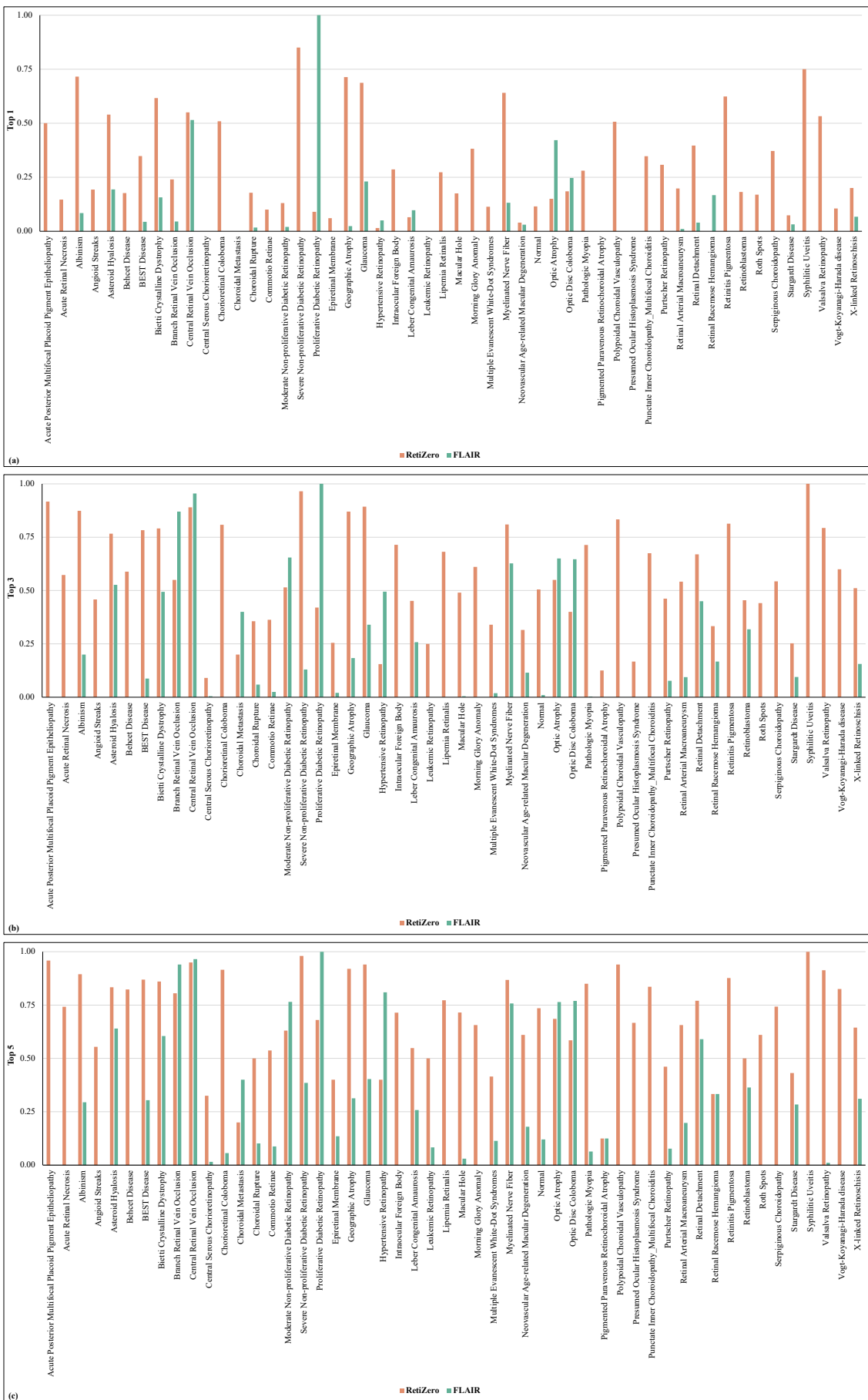
239	Perivasculitis	51
240	Persistent Hyperplastic Primary Vitreous (PHPV)	60
241	Persistent Placoid Maculopathy (PPM)	13
242	Pigment Epithelial Detachment (PED)	97
243	Pigmentary retinopathy	117
244	Pigmented Paravenous Chorioretinal Atrophy (PPCRA)	9
245	Polypoidal Choroidal Vasculopathy (PCV)	76
246	Posterior microphthalmos	2
247	Posterior placoid chorioretinitis	4
248	Posterior scleritis	60
249	Posterior staphyloma	18
250	Posterior uveitis	16
251	Posterior Vitreous Detachment (PVD)	34
252	Pregnancy-associated retinopathy	53
253	Pre-retinal hemorrhage	47
254	Progressive dominantly inherited dystrophy	21
255	Progressive Outer Retinal Necrosis (PORN)	39
256	Progressive subretinal fibrosis and uveitis syndrome	8
257	Progressive systemic sclerodermic retinopathy	1
258	Proliferative Diabetic Retinopathy (PDR)	546
259	Proliferative Vitreoretinopathy (PVR)	201
260	Pseudopapilloedema	9
261	Pseudovitelliform detachment	23
262	Punctate Inner Choroidopathy (PIC)	54
263	Puttscher retinopathy	68
264	Radiation retinopathy	65
265	Reactive lymphoid hyperplasia	6
266	Relentless Placoid Chorioretinitis (RPC)	9
267	Reticular pseudodrusen	15
268	Retinal Angiomatous Proliferation (RAP)	42
269	Retinal arteriovenous malformation	11
270	Retinal artery macroaneurysm	151
271	Retinal break	15
272	Retinal cyst	2
273	Retinal Detachment (RD)	463
274	Retinal dystrophy	7
275	Retinal folds	19
276	Retinal hemorrhage	50
277	Retinal infarction	8
278	Retinal infiltrates	2
279	Retinal ischemia	9
280	Retinal pigment epitheliitis	13
281	Retinal sheathing	8
282	Retinal tear	208
283	Retinal telangiectasia	70
284	Retinal tuft	19
285	Retinitis	54
286	Retinitis Pigmentosa (RP)	302
287	Retinitis punctata albescens	13
288	Retinopathy of Prematurity (ROP)	570
289	Retinoschisis	122
290	Retrobulbar neuritis	1
291	Roth spots	15
292	RPE atrophy	13
293	RPE epithelioma	3
294	RPE hyperplasia	14
295	RPE nevus	7
296	RPE tear	8
297	Sarcoidosis	11
298	Scleritis	1

299	Sclerochoroidal calcification	7
300	Serous retinal detachment	7
301	Serpiginous choroidopathy	143
302	Shaken baby syndrome	63
303	Sickle cell retinopathy	172
304	Silicone oil	46
305	Sjögren Reticular Dystrophy	11
306	Sjögren–Larsson syndrome	2
307	Snailtrack degeneration	18
308	Snowflake degeneration	6
309	Solar/Laser Maculopathy	78
310	Sorsby Pseudoinflammatory Fundus Dystrophy (SPFD)	49
311	Staphyloma	4
312	Stargardt disease	267
313	Stationary night blindness	11
314	Submacular abscesses	1
315	Subretinal fibrosis	14
316	Subretinal fibrosis and uveitis syndrome	28
317	Subretinal hemorrhage	32
318	Sub-RPE hemorrhage	1
319	Suprachoroidal hemorrhage	2
320	Susac syndrome	11
321	Sympathetic ophthalmia	56
322	Synchysis scintillans	2
323	Systemic diseases	70
324	Takayasu retinopathy	4
325	Talc retinopathy	18
326	Terson syndrome	28
327	Tilted disc	44
328	Torpedo maculopathy	8
329	Toxicity	423
330	Toxicity Chalcosis	3
331	Toxicity Siderosis	3
332	Toxicity Tacrolimus microangiopathy	10
333	Tractional retinal detachment	1
334	Transplant-associated retinopathy	7
335	Trauma	81
336	Trauma electrocution retinopathy	3
337	Trauma gunshot	2
338	Trauma optic neuropathy	3
339	Trauma retinal pigment epitheliopathy	6
340	Trauma retinopathy	7
341	Tumor	15
342	Tumor adenocarcinoma of the RPE	3
343	Tumor adenoma of the ciliary body pigment epithelium	2
344	Tumor adenoma of the RPE	19
345	Tumor astrocytic hamartoma	4
346	Tumor cavernous hemangioma	44
347	Tumor choroidal hemangioma	182
348	Tumor choroidal melanoma	512
349	Tumor choroidal metastasis	213
350	Tumor choroidal osteoma	114
351	Tumor choroidal plasmacytoma	2
352	Tumor ciliochoroidal melanoma	29
353	Tumor combined hamartoma of the retina and RPE	117
354	Tumor congenital simple hamartoma of the RPE	2
355	Tumor leiomyoma	1
356	Tumor medulloepithelioma	6
357	Tumor melanocytoma	6
358	Tumor metastasis	4

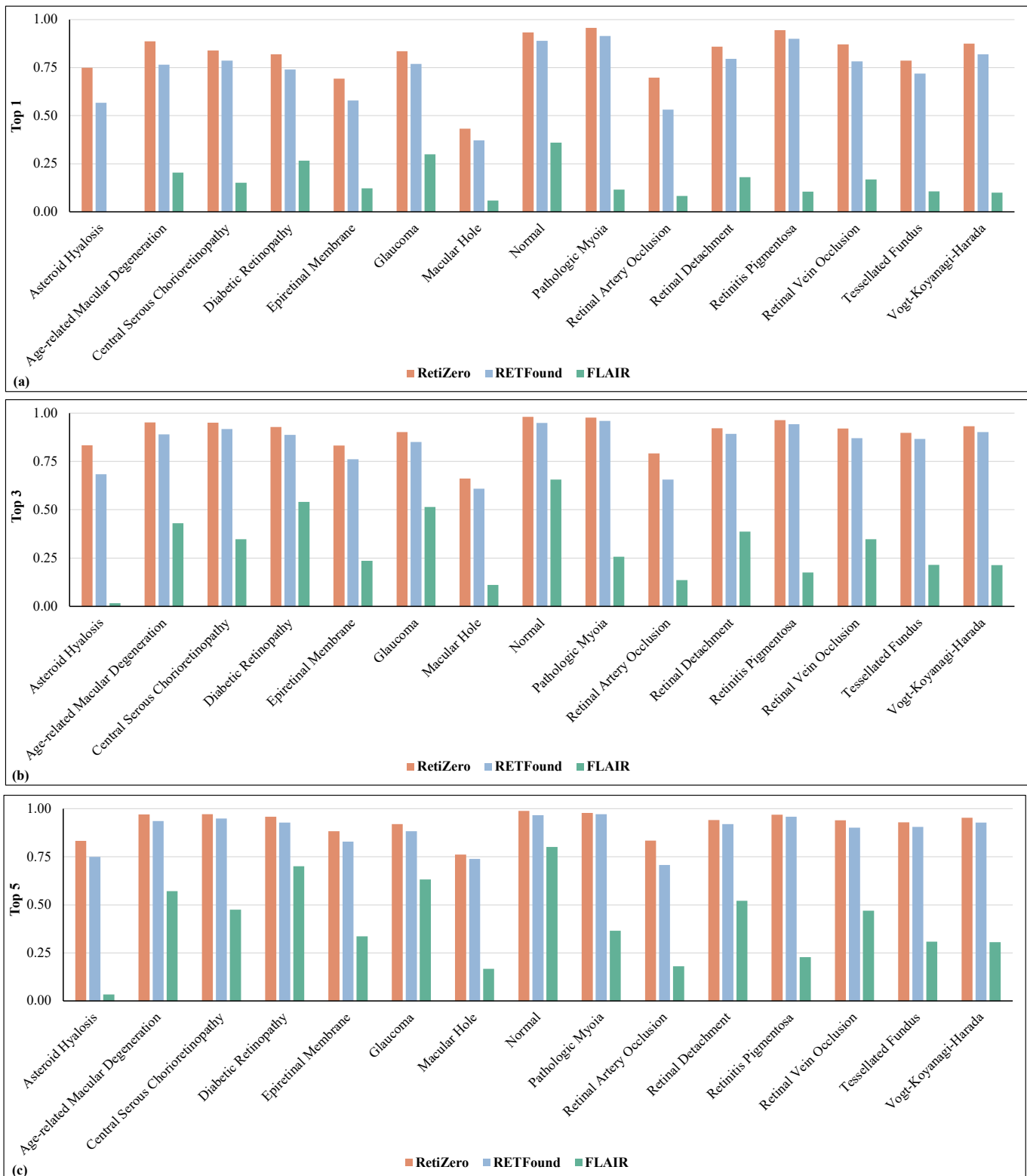
359	Tumor myeloma	2
360	Tumor optic disc astrocytic hamartoma	5
361	Tumor optic disc astrocytoma	6
362	Tumor optic disc capillary hemangioma	15
363	Tumor optic disc glioblastoma	2
364	Tumor optic disc glioma	4
365	Tumor optic disc hemangioblastoma	5
366	Tumor optic disc hemangioma	2
367	Tumor optic disc melanocytoma	104
368	Tumor optic disc melanoma	3
369	Tumor optic disc meningioma	5
370	Tumor retinal angioma	1
371	Tumor retinal astrocytic hamartoma	111
372	Tumor retinal astrocytoma	59
373	Tumor retinal capillary hemangioma	220
374	Tumor retinal cavernous hemangioma	39
375	Tumor retinal hamartoma	2
376	Tumor retinal melanocytoma	1
377	Tumor retinal metastasis	22
378	Tumor retinal racemose hemangioma	25
379	Tumor Retinoblastoma (RB)	513
380	Tumor retinocytoma	7
381	Tumor RPE hamartomas	3
382	Tumor teratoma	1
383	Tumor uveal hemangiopericytoma	1
384	Tumor uveal melanoma	2
385	Tumor uveal metastasis	1
386	Tumor uveal schwannoma	3
387	Tumor Vasoproliferative Tumor (VPT)	48
388	Type 1 aneurysmal telangiectasis	1
389	Type 2 aneurysmal telangiectasis	3
390	Unifocal heliodor choroiditis	1
391	Uveal benign reactive lymphoid hyperplasia	14
392	Uveal Effusion Syndrome (UES)	46
393	Uveitis	46
394	Valsalva retinopathy	59
395	Vascular anomaly	42
396	Vascular sheathing	4
397	Vascular tortuosity	40
398	Vasculitis	99
399	Venous stasis retinopathy	25
400	Vessel shunt	31
401	Vitreomacular Traction syndrome (VMT)	51
402	Vitreous base avulsion	3
403	Vitreous cyst	9
404	Vitreous Hemorrhage (VH)	71
405	Vitreous liquefaction	4
406	Vitreous opacity	15
407	Vitritis	25
408	Vogt-Koyanagi-Harada disease (VKH)	283
409	West African crystalline maculopathy	9
410	West Indies crinkled retinal pigment epitheliopathy	3
411	White with pressure	4
412	White without pressure	10
413	Xerophthalmia	5
414	X-linked juvenile retinoschisis (XLRs)	153
	Total	23,228



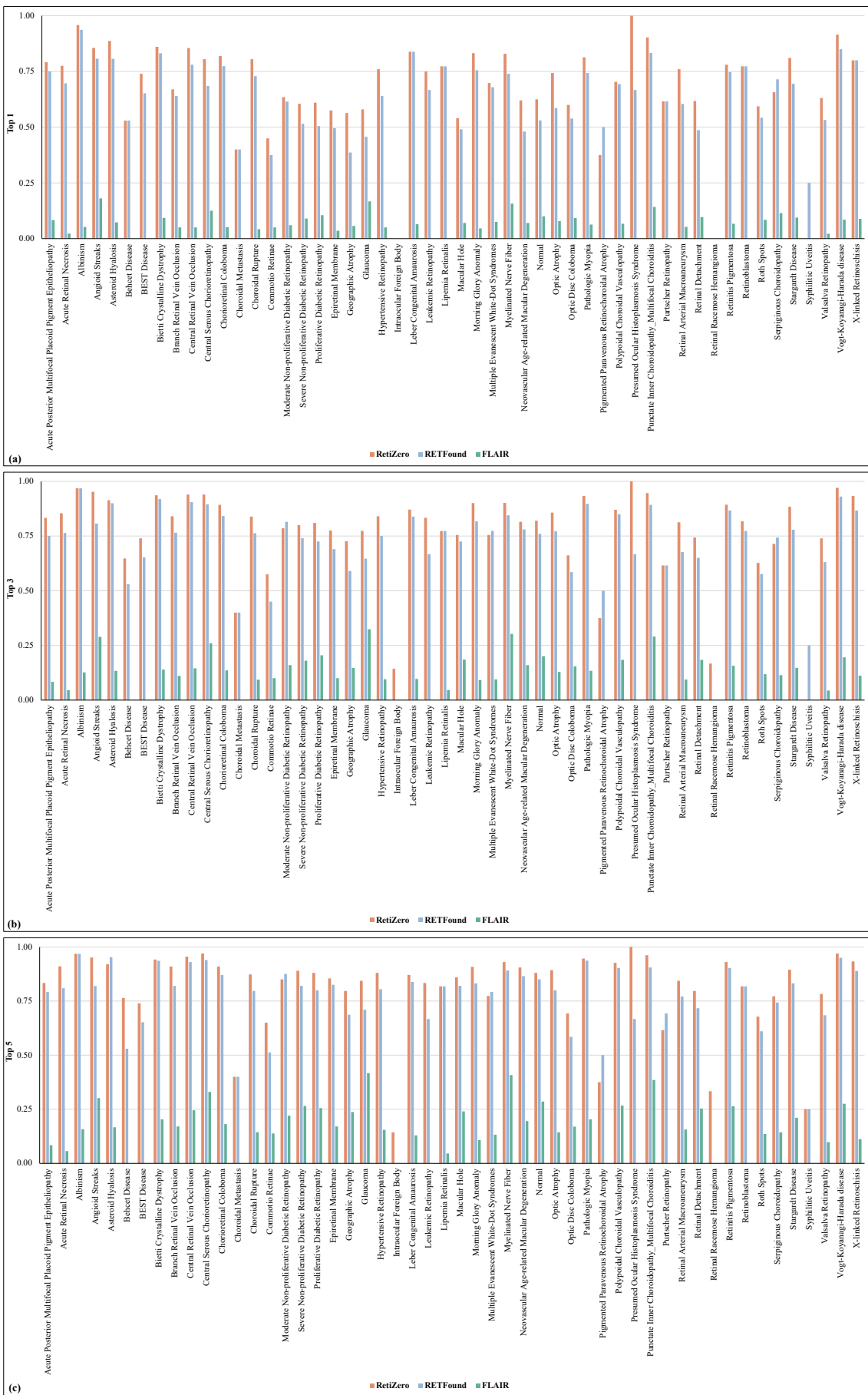
Supplementary Figure 1. Top1, Top3, and Top5 scores of zero-shot recognition for each category in the EYE-15 dataset.



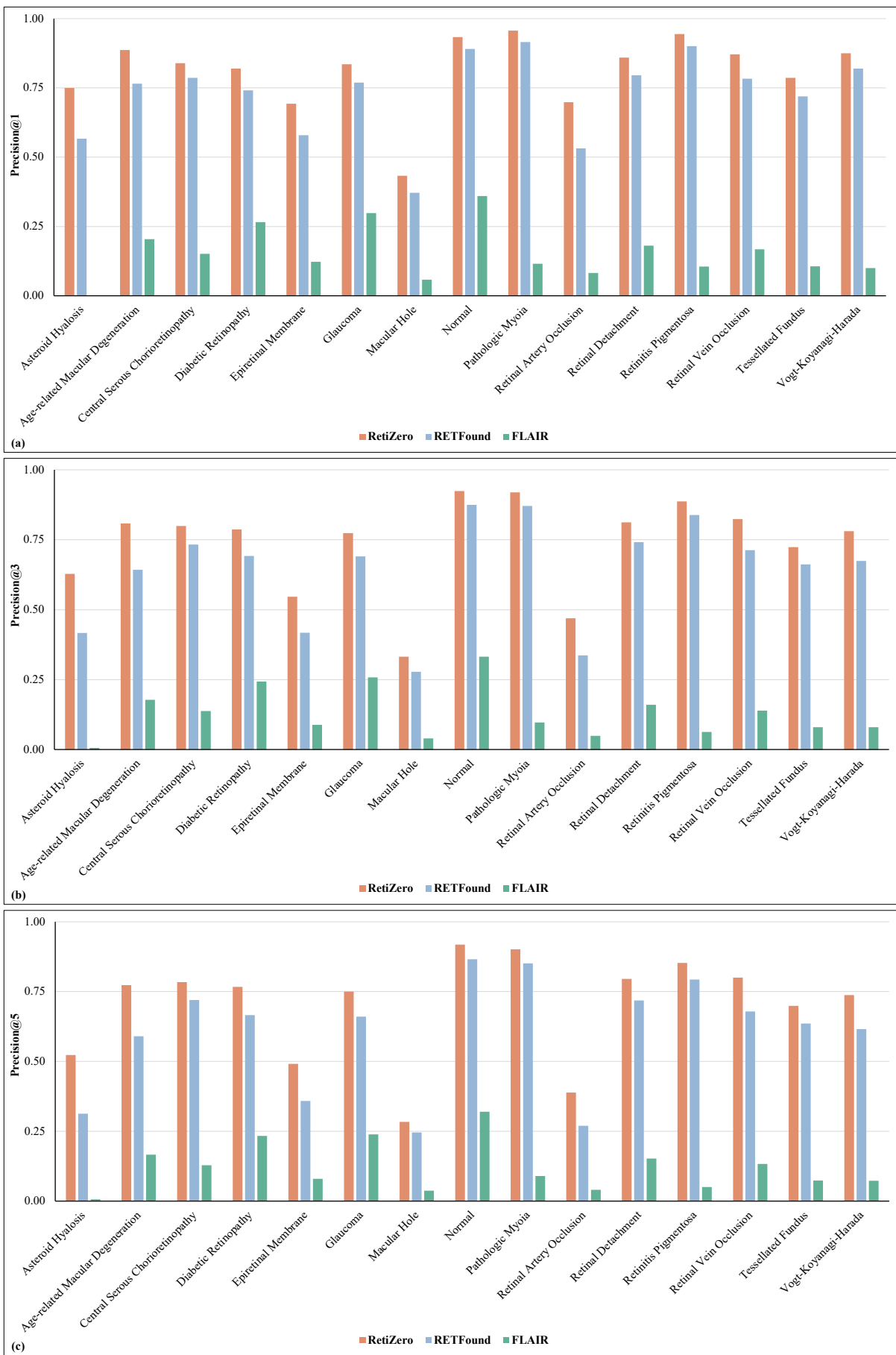
Supplementary Figure 2. Top1, Top3, and Top5 scores of zero-shot recognition for each category in the EYE-52 dataset.



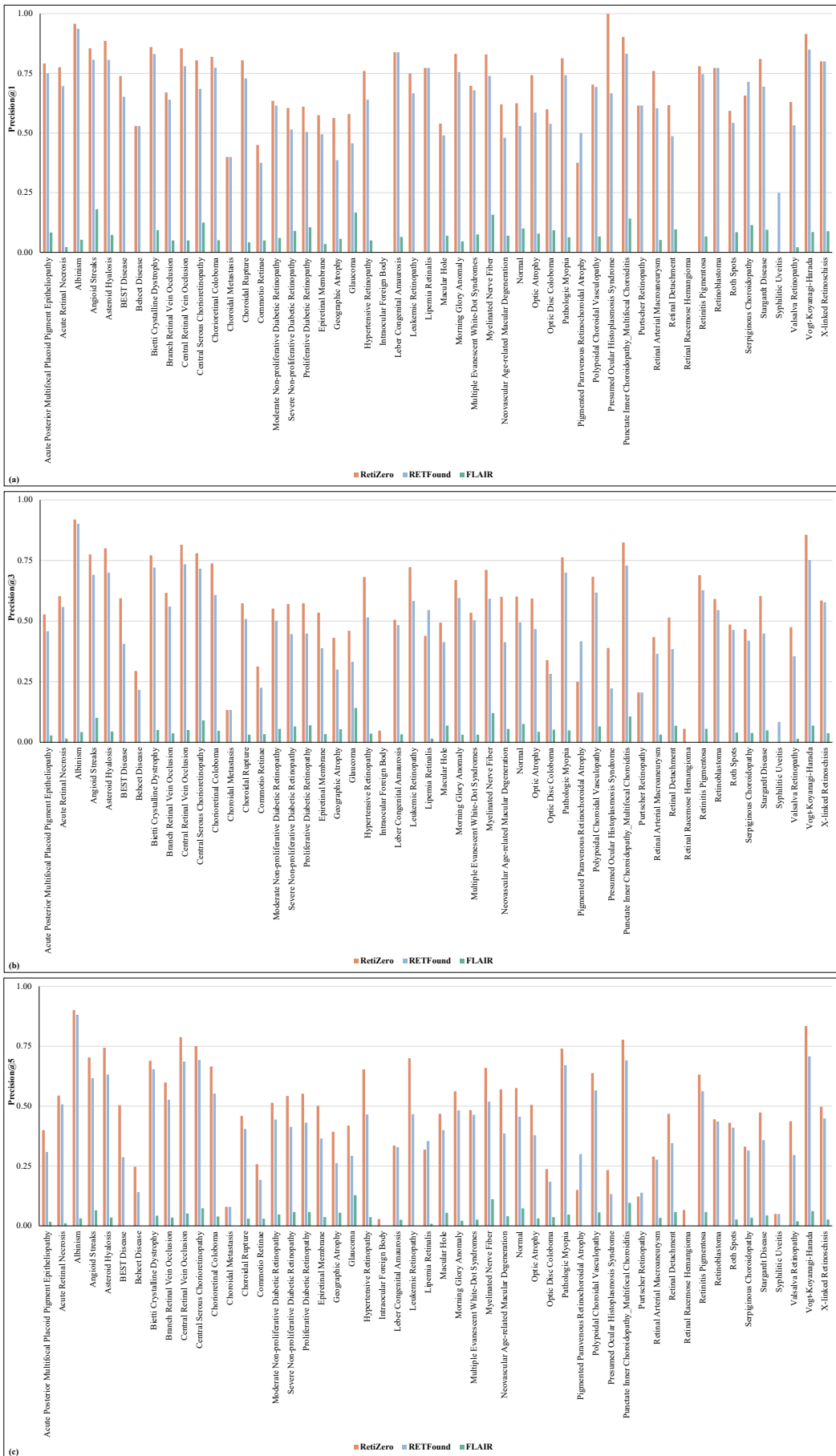
Supplementary Figure 3. Top1, Top3, and Top5 scores of fundus disease identification by image-to-image retrieval for each category in the EYE-15 dataset.



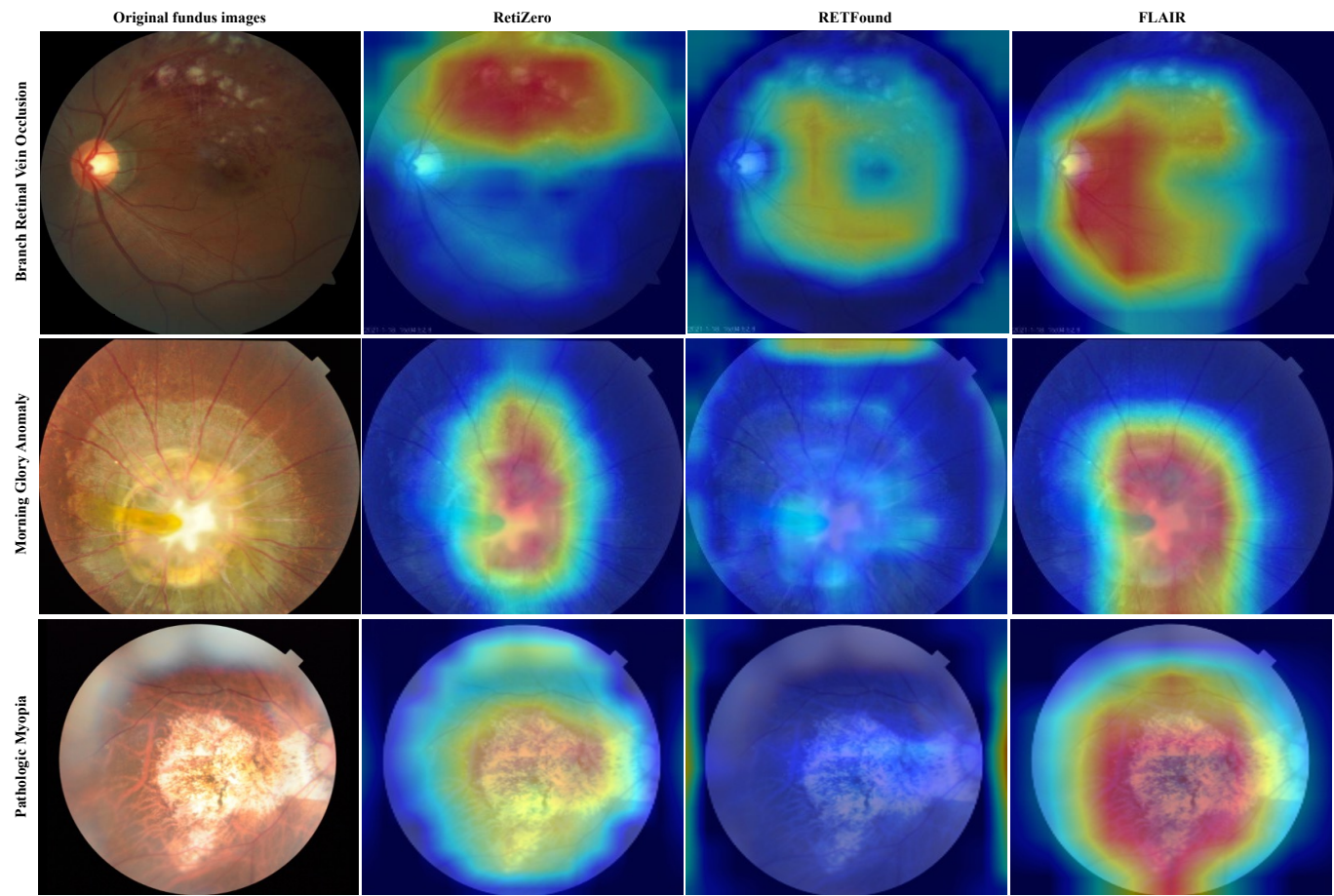
Supplementary Figure 4. Top1, Top3, and Top 5 scores of fundus diseases identification by image-to-image retrieval in the EYE-52 dataset for each category.



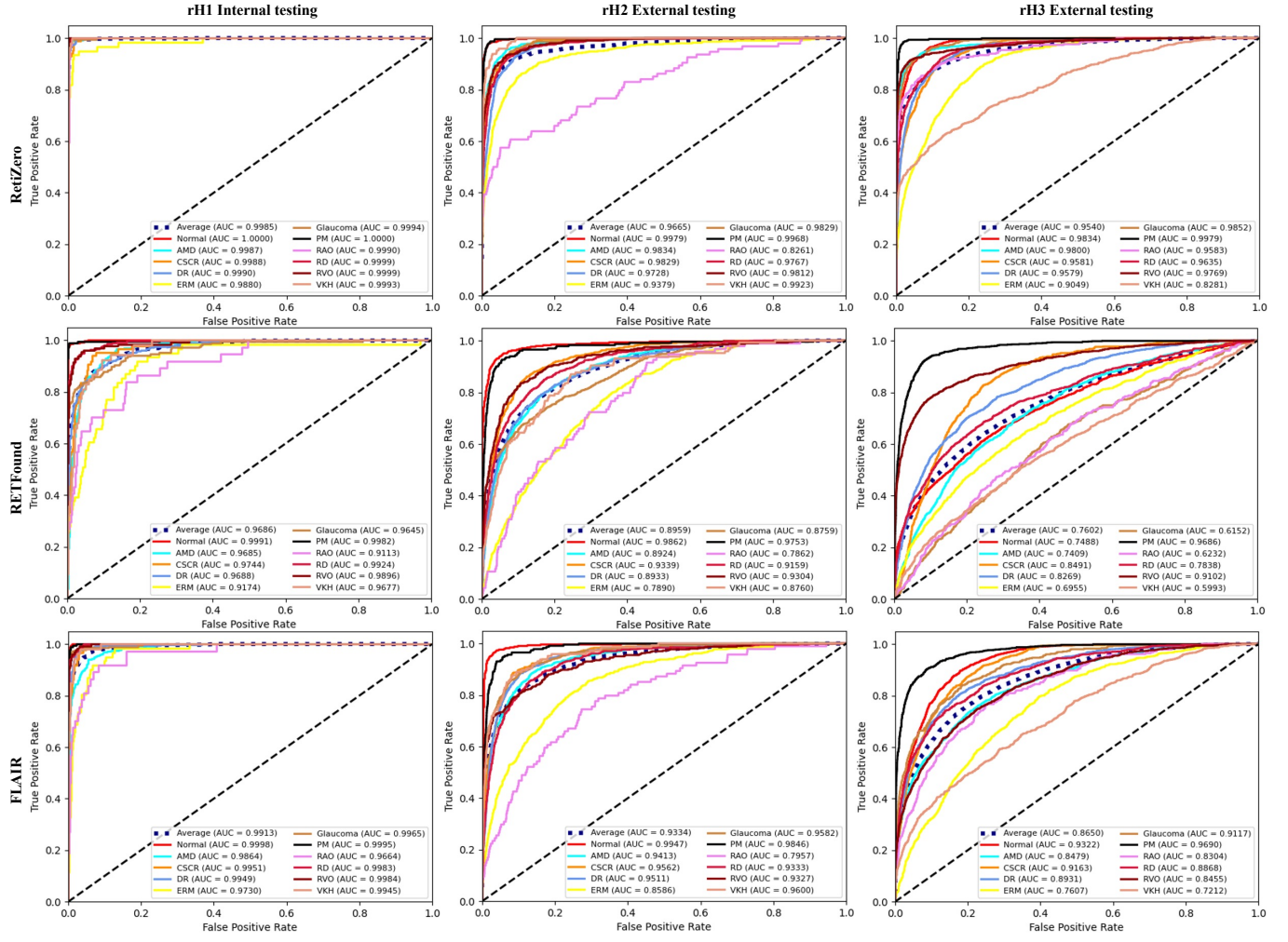
Supplementary Figure 5. Precision@1, Precision@3, and Precision@5 of fundus diseases identification by image-to-image retrieval for each category in the EYE-15 dataset.



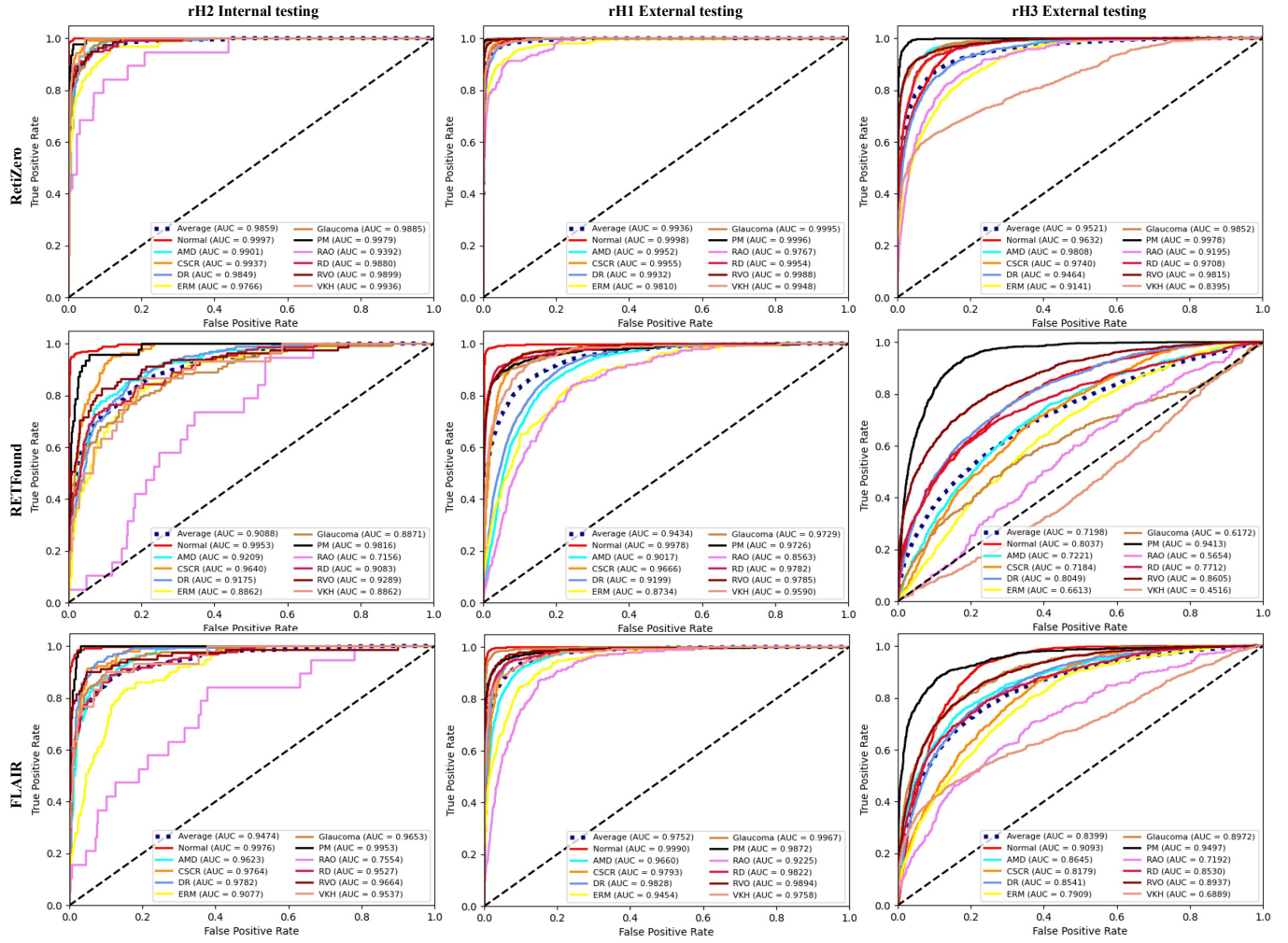
Supplementary Figure 6. Precision@1, Precision@3, and Precision@5 scores of fundus diseases identification by image-to-image retrieval for each category in the EYE-52 dataset.



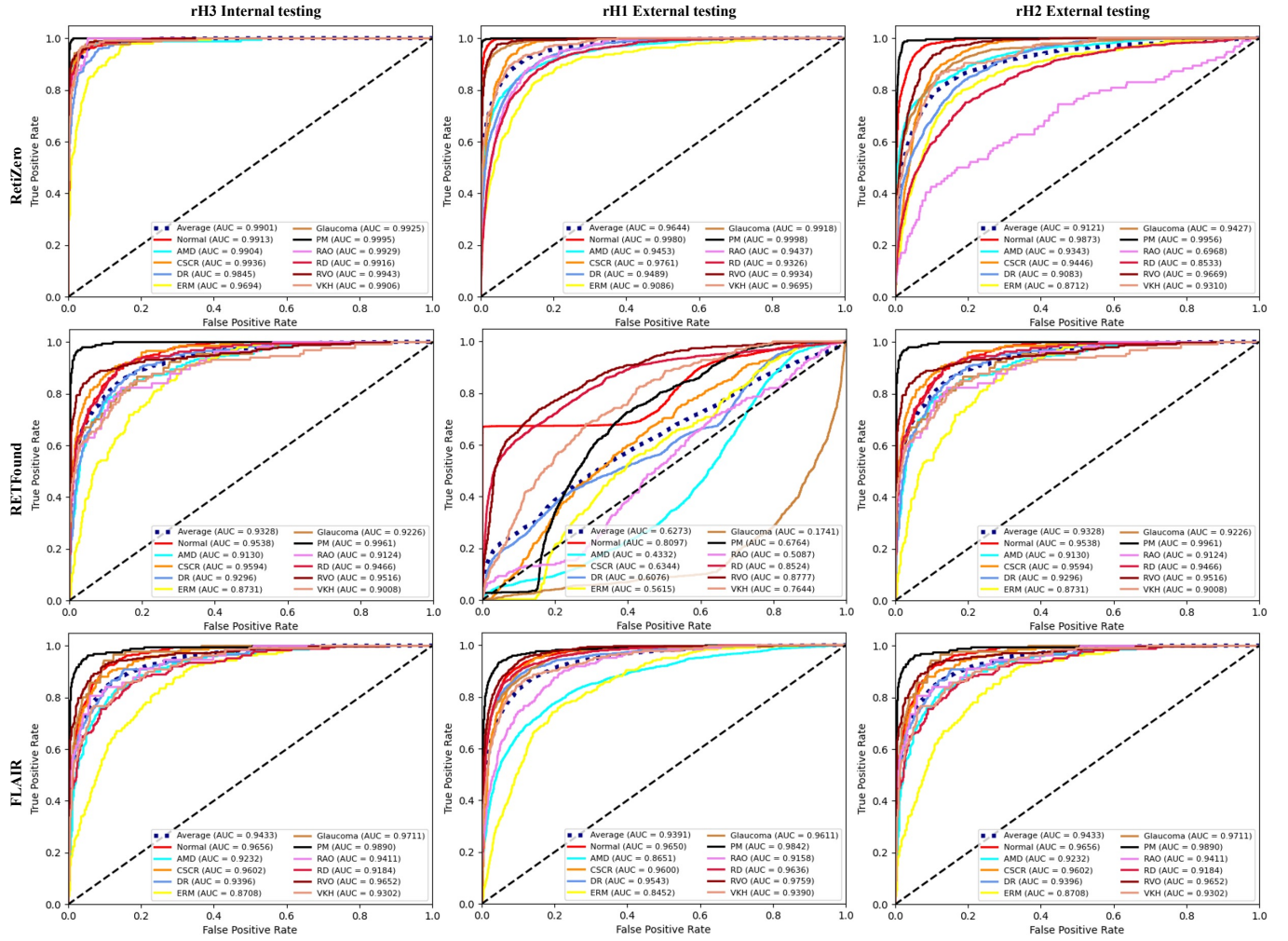
Supplementary Figure: 7. Heatmaps of different foundation model weights for various fundus diseases.



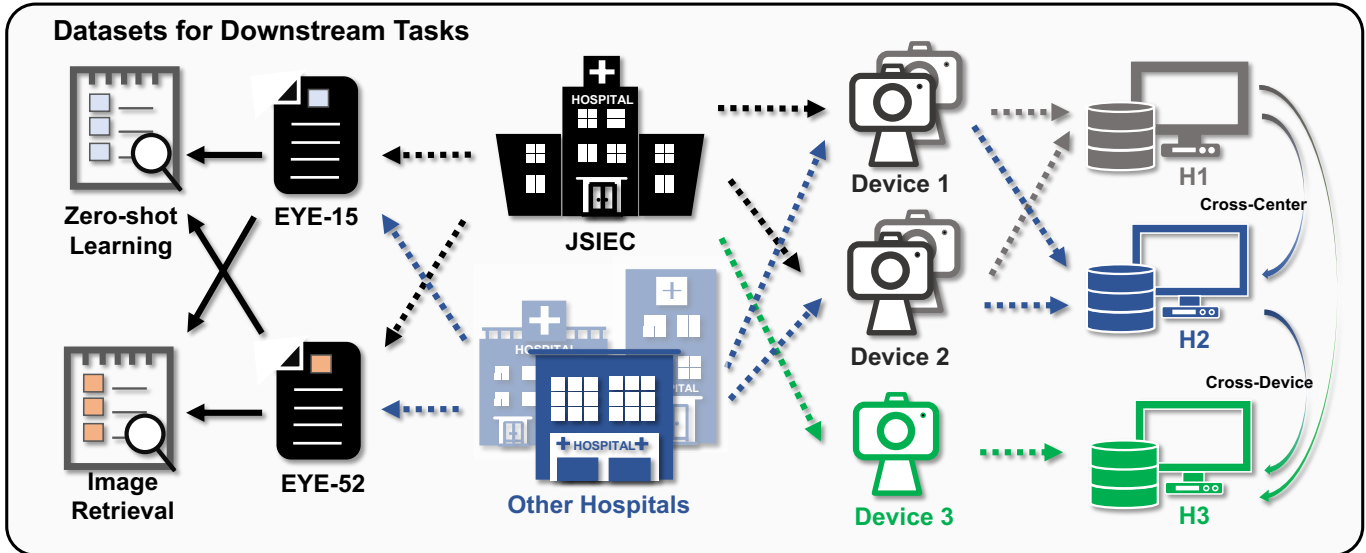
Supplementary Figure 8. AUC scores of different Foundation models on different datasets, where the reorganized rH1 dataset was adopted as an internal set, while both reorganized rH2 and rH3 datasets were used as external test sets.



Supplementary Figure 9. AUC scores of different Foundation models on different datasets, where the reorganized rH2 dataset was adopted as an internal set, while both reorganized rH1 and rH3 datasets were used as external test sets.



Supplementary Figure 10. AUC scores of different Foundation models on different datasets, where the reorganized rH3 dataset was adopted as an internal set, while both reorganized rH1 and rH2 datasets were used as external test sets.



Supplementary Figure: 11. For the downstream tasks, we divided the datasets as follows: H1 comprised devices 1 and 2 of JSIEC, H2 consisted of devices 1 and 2 from four other medical centers, and H3 included data from device 3 of JSIEC. Additionally, we collected data from devices D1 and D2 of all medical centers to form the EYE-15 and EYE-52 datasets, respectively.